POLITECNICO
MILANO 1863

SCUOLA DI INGEGNERIA INDUSTRIALE
E DELL'INFORMAZIONE

Design and fabrication of an integrated photonic circuit for the generation of heralded three-photon entangled states

Tesi di Laurea Magistrale in
Engineering Physics

Author: **Valerio Galli**

Student ID: 10578713
Advisor: Prof. Roberto Osellame
Co-advisors: Hugo Ferreira
Academic Year: 2022-2023

Abstract

The research to develop a quantum computer is going on from many years now. Different solutions have been proposed, each with its pros and cons. One of these employs photons as qubits and is called *One-way quantum computing*. Only linear optical components, already existing, acting on only one photon at a time, are necessary to implement this solution. The difficulty lies in generating the so called *cluster* state, an entangled state of many photons, which is needed, before everything else, to implement this particular protocol. For the generation of such state, the basic building block is a three-photon entangled state, called GHZ state. During this work, an integrated optical circuit for the generation of GHZ states has been designed and fabricated. The circuit works with six photonos, three will generate the GHZ state and the other three will act as heralders: when a precise outcome is obtained from their measurement, it ensures that the other three photons are in the correct state.

The technique used to fabricate this photonic circuit was *Femtosecond laser micromachining*, through which ultrashort laser pulses are tightly focused in a glass substrate, inducing permanent modifications. These modifications allow us to fabricate all the optical components needed to build our device. Two different borosilicate glass substrates were used to achieve this goal. We could not achieve a consistent performance with Borofloat, but the data gathered highlighted the fact that it is possible to fabricate integrated optical devices with very low losses in this glass; to do this further investigation is certainly required. On the other hand in EagleXG glass a complete device for the generation of heralded GHZ states has been fabricated successfully and validated by different characterizations. Further testing will be performed with single photon sources, required by the device to produce the desired state.

Keywords: Integrated photonics, one-way quantum computing, entanglement, GHZ state, femtosecond laser micromachining, Borofloat, EagleXG

Sommario

La ricerca per lo sviluppo di un computer quantistico sta continuando da ormai molti anni. Diverse soluzioni sono state proposte, ognuna con i propri pro e contro. Una di queste utilizza i fotoni come qubit ed è denominata *one-way quantum computing*. Solo elementi ottici lineari, già esistenti, che svolgono operazioni su un singolo fotone alla volta, sono necessari per implementare questa soluzione. La difficoltà risiede nella generazione del così chiamato stato *cluster*, uno stato entangled composto da molti fotoni, il quale è necessario, a valle di tutti gli altri elementi, per implementare questo particolare protocollo. Per generare questo stato l'elemento base è uno stato entangled a tre fotoni, chiamato stato GHZ. Durante questo lavoro di tesi, un circuito ottico integrato per la generazione di stati GHZ è stato progettato e fabbricato. Il circuito agisce su sei fotoni, tre genereranno lo stato GHZ e gli altri tre fungeranno da araldi: quando questi ultimi vengono misurati in una precisa distribuzione, garantiscono che gli altri tre siano nello stato corretto.

La tecnica usata per fabbricare questo circuito fotonico è stata la *microfabbricazione con laser a femtosecondi*, attraverso la quale impulsi laser ultrabrevi vengono focalizzati in un substrato vetroso, inducendo una modifica permanente nel vetro. Queste modifiche ci permettono di fabbricare tutti i componenti ottici necessari per implementare il nostro dispositivo. Due differenti vetri in borosilicato sono stati usati per raggiungere questo obiettivo. Non siamo riusciti ad ottenere dei risultati consistenti con Borofloat, ma i dati raccolti hanno evidenziato il fatto che è possibile fabbricare dispositivi ottici con perdite molto basse in questo vetro; per farlo sono sicuramente necessarie ulteriori ricerche. D'altra parte nel vetro EagleXG è stato fabbricato con successo, e validato da successive caratterizzazioni, un dispositivo completo per la generazione di stati GHZ con araldi. Ulteriori test verranno svolti con sorgenti di singolo fotone, necessari al dispositivo per generare lo stato desiderato.

Parole chiave: Fotonica integrata, one-way quantum computing, entanglement, stato GHZ, microfabbricazione con laser a femtosecondi, Borofloat, EagleXG

Contents

1 | Entangled state and quantum computing

In this chapter is given an introduction about quantum computing, in particular how photons can be exploited to achieve it. One-way quantum computing is briefly described, to understand the relevance of the cluster state. The last section is focused on the Greenberger-Horne-Zeilinger state and its importance for quantum computing. A description of this state is given, focusing also on its generation, which is the final purpose of this work.

1.1. Introduction to quantum computing

This section comprehends a general overview of the basic building blocks of quantum computing. It begins with a description of the qubit, where the information is encoded; then proceeds with its manipulation. The last paragraph deals with quantum entanglement, a phenomenon which is at the basis of this thesis work and also of photonic quantum computing itself.

1.1.1. Quantum Bit: the basic block of information

In classical computers the information is encoded in bits. They can assume the logical values of 0 or 1. These values are usually related to electrical signals, for instance a voltage or a current. These days the technology to manipulate bits, read their value and perform operations on them is well know. It relies on transistors, which are basically voltage controlled switches.

In quantum computers the information is encoded in qubits (quantum-bits). A qubit can assume the logical value 0 or 1 when measured, as classical bits. These are associated to quantum states that can be written for simplicity as $|0\rangle$ and $|1\rangle$. These logical values are related to some physical quantities and this choice is arbitrary. Examples of encodings are orthogonal polarizations or physical path. For instance if one has two different physical paths the state $|0\rangle$ may correspond to the presence of a photon in the first path and the

state $|1\rangle$ to the presence of a photon in the second path (this is named dual-rail path encoding). Regardless of the type of encoding chosen, the two states must be orthogonal and form a complete basis [2]. Up to here seems that qubits have no advantage with respect to classical bits, but the relevant difference lies in the possibility of having a superposition of states, which is a characteristic of quantum states only. To understand this we can write the general expression of a qubit, which is the superposition of the two logic states:

$$|\Psi\rangle = \cos\left(\frac{\theta}{2}\right)|0\rangle + e^{i\phi}\sin\left(\frac{\theta}{2}\right)|1\rangle \tag{1.1}$$

It is easier to visualize this in the 3D representation of the Bloch's sphere, as shown in Figure 1.1.

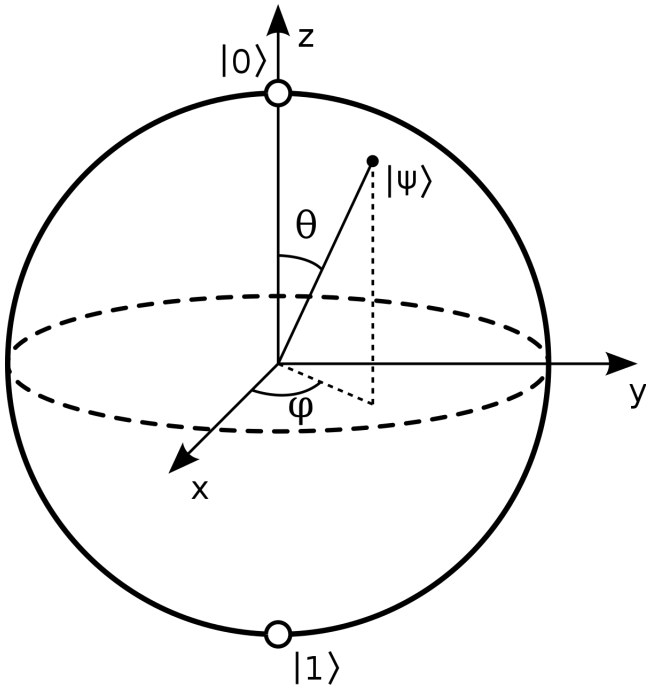

Figure 1.1: Bloch's sphere, visual representation of qubits. The sphere has unitary radius. Each state can be represented in the basis $\{|0\rangle,|1\rangle\}$ through the angle θ. The angle ϕ is a global phase. Every unitary operation on a qubit correspond to a rotation on the sphere.

A single qubit can be any of the infinite points on the sphere's surface, so in principle it can contain infinite information, this is the main difference with respect to classical bits. The ability to simultaneously manipulate multiple qubits in a superposition of states allows to speed up the computation of some algorithms. To exploit this is not so straightforward, because when a measurement is performed on a qubit its wavefunction collapses, either

on state $|0\rangle$ or $|1\rangle$, so all the information encoded is lost. The cleaver way to exploit qubit superposition and measurements, to perform faster calculation, is the foundation of quantum computing.

Now I'll focus on qubit manipulation. Again, let's start from classical bits. They can be manipulated with logic gates, which accept one or more bits as inputs and give one or more bits as outputs. The only classical one-bit gate that exist is the NOT gate: it changes the value of the bit received as input. Two-bit gates perform well known logical operation like AND, OR, XOR and give as output a single bit. There are other examples of possible operation in classical computing and they can all be implemented with electrical circuitry with ease. Since any of these gates can be realized with transistors, we are able to implement every classical algorithm on a classical computer.

For quantum computers can be demonstrated that every algorithm can be implemented using a number of single-qubit gates and only one two-qubit gate [2]. To understand this we write the qubit in a simpler notation, so as to be able to describe the gates with a simple matrix. A general qubit can be written as

$$|\Psi\rangle = C_0 |0\rangle + C_1 |1\rangle = \begin{pmatrix} C_0 \\ C_1 \end{pmatrix} \tag{1.2}$$

with

$$C_0^2 + C_1^2 = 1 \tag{1.3}$$

to ensure we have a unitary vector. The modulus squared of each coefficient is the probability to observe the corresponding state, when a measurement is performed on that qubit. With this notation it is possible to write any gate in a matrix form, in particular a unitary matrix, which preserves the unitary modulus of the vector on which it is applied. As stated before any qubit is a point on a unitary radius sphere and any unitary operation is a rotation of it. In general a single qubit gate can be written:

$$\begin{pmatrix} C_0' \\ C_1' \end{pmatrix} = \begin{pmatrix} M_{1,1} & M_{1,2} \\ M_{2,1} & M_{2,2} \end{pmatrix} \begin{pmatrix} C_0 \\ C_1 \end{pmatrix} \tag{1.4}$$

There is more than one single-qubit gate, that is because we do not have just two possible values for a qubit, but infinite. The most relevant single qubit gates are the X-gate (quantum NOT), the Z-gate and the H-gate (Hadamard). Their matrix representation is

shown in Equation 1.5.

$$\mathbf{X} = \begin{pmatrix} 0 & 1 \\ 1 & 0 \end{pmatrix} \qquad \mathbf{Z} = \begin{pmatrix} 1 & 0 \\ 0 & -1 \end{pmatrix} \qquad \mathbf{H} = \begin{pmatrix} 1/\sqrt{2} & 1/\sqrt{2} \\ 1/\sqrt{2} & -1/\sqrt{2} \end{pmatrix} \tag{1.5}$$

The X-gate flips the logic state. The classical NOT gate is embedded in it, but it acts also on superposition of states. The Z-gate adds a π phase shift on the coefficient correspondent to the $|1\rangle$ state. The Hadamard gate creates a superposition of states from the computational basis or it does the inverse operation. The physical realizations of these single-qubit gate is simple, it relies on beam splitters, polarizing beam splitters and half-wave plates. For example, considering polarization encoding, if we want to perform a NOT gate on a photon, we just need a half-wave plate at an angle of 45° with respect to the chosen polarization direction. A simple scheme is depicted in Figure 1.2.

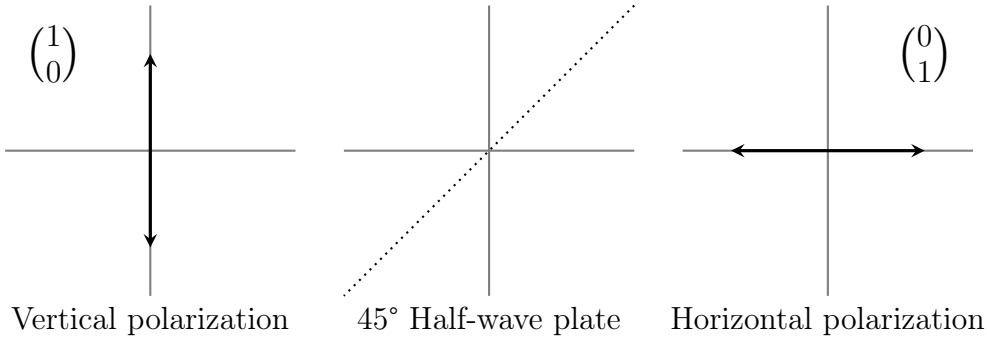

Figure 1.2: Physical implementation of a NOT gate, for polarization encoded photon qubits. Starting from vertical polarization, passing through a 45° half-wave plate, horizontal polarization is obtained. With the proposed encoding this correspond to apply a NOT gate to the state. This remains true also in reverse.

In quantum computers any operation is completely reversible (except for the final measurement): applying the inverse matrix we can recover the initial qubit value. This is totally different from classical computers. As expected, if several operations are performed in sequence on a qubit, the matrix describing the composed operation is just the product in sequence of all the matricies of the operations involved.

About two-qubit gates the machinery is the same, we just have to write the two-qubit state as

$$|\Psi\rangle = C_{00}\,|00\rangle + C_{01}\,|01\rangle + C_{10}\,|10\rangle + C_{11}\,|11\rangle = \begin{pmatrix} C_{00} \\ C_{01} \\ C_{10} \\ C_{11} \end{pmatrix} \tag{1.6}$$

A two-qubit gate can be represented by a 4x4 matrix, which will act on the 4 coefficients used to describe the two-qubit state. An example of two-qubit gate is the Controlled-NOT gate, shown in Figure 1.3.

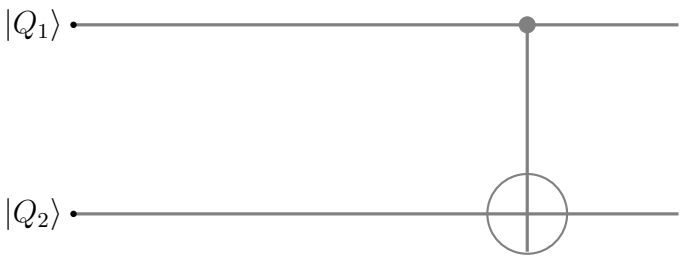

Figure 1.3: C-NOT gate visual representation. The information stored in in the qubits travels to the output along the horizontal lines. The gate is represented by the vertical line and the circle with a cross. The latter is a NOT gate, but controlled by the value of the qubit travelling through the black circle, to which it is connected.

This gate apply a NOT operation to the qubit Q_2 when the qubit Q_1 has logical value 1. Having the possibility for qubits to be in a superposition of states, the output and the implementation of this gate become complicated. The C-NOT gate, as any other two-qubit gate, is an entangling gate. The two qubits that go through the gate will interact and become entangled. This entanglement is crucial for quantum computing and will be discussed it in the next paragraph.

1.1.2. The relevance of Entanglement

Entanglement is one of the most intriguing characteristics of quantum mechanics. There is no classical equivalent for this phenomenon. A lot of discussions regarding entanglement have been carried out in the last century, involving some of the best minds in Physics. This phenomenon challenges realism and locality, on which physics, and moreover the scientific method, has always been based on.

A state of two particles is said to be entangled if it cannot be written as the product of two different state of each single particle. A simple example is the output state of the C-NOT gate of the previous paragraph:

$$CNOT\left[\left(\alpha\left|0\right\rangle+\beta\left|1\right\rangle\right)\left|0\right\rangle\right]=\alpha\left|00\right\rangle+\beta\left|11\right\rangle \tag{1.7}$$

The NOT gate is applied to the qubit in the state $|0\rangle$, only if the control qubit is in the state $|1\rangle$. Nevertheless the control qubit is in a superposition of state, so the result of this operation is the one written in the equation. It is not a separable state, it is a superposition of two states in which the qubits can assume only value $|00\rangle$ or $|11\rangle$. Since they are entangled, we cannot know the outcome that we have obtained unless we measure them. But if we measure one of them, we know also the state of the other one. Measuring only one of them makes the wavefunction of the other collapse in a precise state, even if nothing interacts with it, even if it is far away from the one measured.

The previous statement sounds counterintuitive and it bothered many physicist (such as Einstein). Different theories were proposed to explain it, without losing the principles on which physics has always been based on [11]. The most famous theory is the Local Hidden Variables one. It states that the correlation is present before the measurement; the state of the particles is already defined, but we do not have access to it. This theory does not violate realism, because the state is always defined, we just do not know it; and does not violate locality because there is no need for communication between the two particle to choose the state. This theory has been disproven by different experiments, usually relying on the Bell's inequality [14]. This was a great achievement for quantum mechanics. The wave function that we are able to write, which gives just probabilities of finding the system in a certain state, is not a matter of our lack of information, is the best that can be written, it is how the universe works. Some "loopholes" were raised to not abandon the old description of things. They were again disproven, apart for the last one of them that still holds, which is the absence of free will. This really is the last resort, there are no experiments today that are able to prove the presence or absence of free will. I don't think that we need to push ourselves this far to prove the validity of quantum mechanics. In the context of this thesis, seen the impossibility to prove free will, we will proceed assuming quantum mechanics to be non-local and non-real.

As already stated, a two-qubit gate provides an entangled state at its output. This is necessary, since we must use two-qubit gates to build our algorithm. There are different ways to implement a qubit, the reader is referred to [15] for comprehensive review. Each have its advantages and disadvantages, but for any of them entanglement is needed to implement any algorithm.

In this work single photons are used as qubits, with path encoding. It is very easy to implement practically single-qubit gates for photons. It is much more difficult to create

a two-qubit gate. Photons hardly interact. This is a strength regarding their coherence, they have very long coherence time with respect to other qubit technologies. On the other hand, when we want photons to interact to build a two-qubit gate, we encounter a huge problem. To overcome this, generating entanglement at the beginning of the computation is the solution. This is why entanglement is so relevant for photonic quantum computing and in the next section this will be explained in details.

1.2. Platforms and paradigms in quantum computing

In this section, after a brief introduction on quantum computing, the photonic approach to it will be presented. The paradigm of One-way quantum computing is presented, which relies on a cluster state, an entangled state with many photons. This eliminates the need of two-qubit gates and so reduces the realization of a photonic quantum computer to only single-qubit gates, which have been already demonstrated in different platforms.

1.2.1. Linear optical quantum computing

It has been shown, in the past decades, that, for certain classes of problems, quantum computing is the next step to pursue, to implement new algorithm or speed up the existing ones. The theory behind quantum computing is already developed for some problems. A famous examples that shows its power is Shor's algorithm (to factorize large number). It is an irrefutable proof that with quantum computing is possible to solve problems which cannot be afforded classically.

In optical quantum computing the chosen qubits are photons. Their clear advantage is their strong coherence, which is a very relevant factor and a big problem in other approaches. This means that photons remains in their state for long times, so they can store information without any concern to lose it. Moreover a single photon is the smallest unit of quantum information and it is also highly compatible with all the modern communication technologies. On the downside photons do not interact with other photons, which makes it difficult to build two-qubit gates.

Different approaches were proposed. At the beginning non linear processes were exploited, like second harmonic generation, but they require very high pump powers and their efficiency is low. Then a new protocol was developed, to bring the non-linearity of the quantum gates to the state [21]. The KLM protocol, therefore, opened the way for linear optical quantum computing (LOQC) [22]. It basically removes the needs of having photons interacting between them, reducing all the machinery needed to implement every

algorithm to single-qubit gates, which as already said, are easy to realize. Using photons as qubits also allows us to resort to integrated optics, which allows for miniaturization and integration. This is needed to scale-up the devices and further improvements.

1.2.2. One way quantum computing

From what has been said, LOQC seems very simple to implement, but it is not. The original KLM proposal involved quantum teleportation, which is not practical. To remove the necessity of making photons interact, an initial state of entangled photons is required. Has already been said a two-quibit gates produces entanglement between photons, so we can avoid using it by starting from a huge amount of photons already entangled. This is called a cluster state. The cluster state serves as a universal substrate, on which any algorithm can be performed, provided the presence of enough photons. The algorithm is imprinted on the cluster state by performing only single-photon measurements. Two-qubit gates are not needed, as demonstrated in [32]. The initial entanglement is reduced by every measure, up to the end where the final result is obtained. This process is called *one-way quantum computing*, because starting from a cluster state, a single measurement is performed on each photon, with a particular sequence, to obtain the final result with just one series of operation.

While protocols for errors correction have already been developed [44], it has also been shown [45] that is possible to achieve computation with single photon sources and imperfect detectors. If the product of their efficiency is greater than $2/3$, then efficient quantum computation is possible. State of the art technology allows for such values.

Therefore, the biggest challenge for one-way quantum computing is to produce the cluster state. A protocol to achieve this cluster state is described in [23]. It shows that such state can be built from basic building blocks states. In each of these building block states, there is one photon which is the actual qubit carrying information. Other photons are entangled to it in a tree configuration. This unit with multiple photons is needed both for error correction, as shown in [44], and to join the blocks together in the cluster state. To do so Briegel and Raussendorf [6] proposed a fusion protocol, that allows to join together different entangled photons in a single entangled state. This requires a measurement on some of the photons of the block. This destroys the entanglement, as any measurement in quantum physics, that is why building blocks with multiple photons are needed.

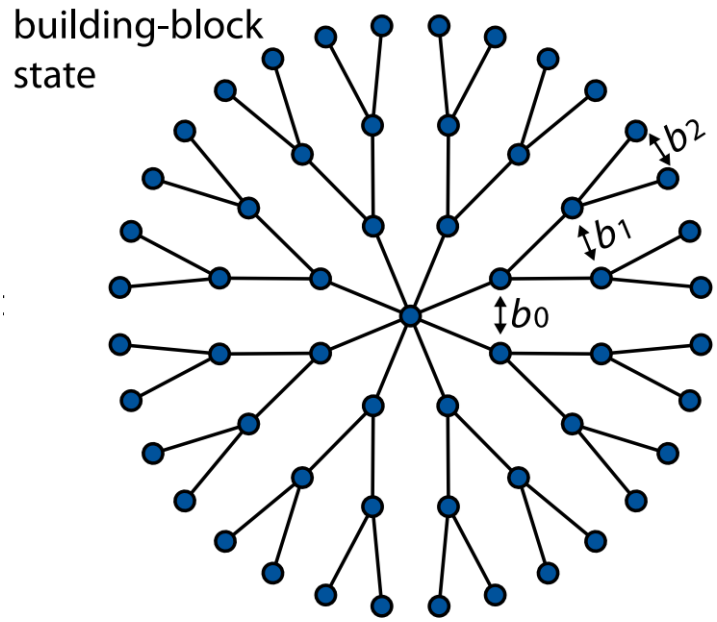

Figure 1.4: Building block state for cluster state. The indexes b_i are branching numbers, they are the number of the i-th generation branches of the bridge unit. Image taken from [23]

Type-II fusion is used also in the first step to build the cluster. It starts with a three photons entangled state, the Greenberger-Horne-Zeilinger state (GHZ). Because the type-II fusion involves a measurement on a photon of two different aggregates, if we start with less than three entangled photon on each group, we are not able to join them together in larger groups. This highlights the importance of the generation of the GHZ state; for a deeper discussion about its relevance refer to [36]. In particular we need a high ratio of generation of this state. This is because we want a lot of them to be joined together in a cluster state, which comprehends thousands of photons, to be able to implement every algorithm in our photonic quantum computer. The work done in this thesis aims at the generation of GHZ states.

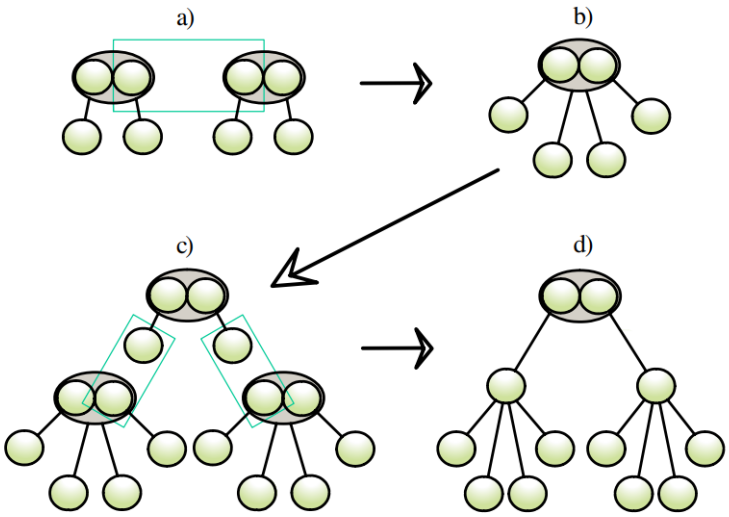

Figure 1.5: Scheme of type-II fusion protocol to build tree cluster, starting from GHZ states. Each circle corresponds to a photon, the light blue rectangles represent the measurements. It is possible to join entangled states together to form bigger and bigger entangled state. Image taken from [45]

1.3. The Greenberger-Horne-Zeilinger state

In this section will be described the GHZ state from a theoretical point of view. Its applications will be pointed out and the requirements necessary for the state generation.

1.3.1. Description and importance

This state was first proposed by the three scientist from which it takes its name [16]. The Greenberger-Horne-Zeilinger states are maximally entangled three-photon states [3], which means they maximally violate the Bell's inequality. The properties of maximally entangled states, such as that states obtained from them are still maximally entangled, are discussed in [14].

In the qubit basis the GHZ state can be expressed as:

$$|GHZ\rangle = \frac{1}{\sqrt{2}}(|000\rangle + e^{i\phi}|111\rangle) \tag{1.8}$$

Being this an entangled state, measuring one photon makes the wavefunctions of the other two collapse in the correspondent state, which can be only $|000\rangle$ or $|111\rangle$. A simple scheme to achieve this state is depicted in Figure 1.6.

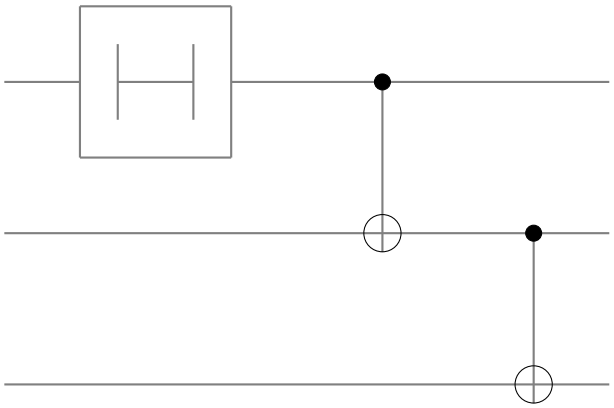

Figure 1.6: GHZ state generation scheme with one and two qubit gates

The scheme consist in a single-qubit Hadamard gate and two two-qubit C-NOT gates. Entering from the left with three qubits in the $|0\rangle$ or $|1\rangle$ states, the output is exactly the GHZ state defined in Equation 1.8. However, as discussed in the previous sections, a photonic implementation of two-qubit gates is difficult, so the aim of this work is to fabricate a device that can generate a GHZ state to avoid the use of such gates.

A last remark before describing a functioning generation scheme for the GHZ state. This particular state is not only useful for the generation of cluster states, but has also other application in quantum communication and quantum cryptography [2][12]. Last but not least, it is also useful for experiments involving the Einstein-Podolsky-Rosen paradox [11] and the Bell's inequality [14], which put to the test the most exotic properties of quantum mechanics.

1.3.2. Overview of GHZ generation schemes

In the last twenty-five years different schemes for the generation of the GHZ state were proposed and implemented. One of the first ones was proposed by Zeilinger et al. [46]. In this article they explained how to produce a GHZ state, starting from two couples of entangled photons and performing a measurement on one particular photon. The scheme for this is depicted in Figure 1.7. Two sources of entangled photons pairs emits simultaneously. A measurement is performed at the detectors D_T and D'_T, after a 50/50 beam splitter. If only one detector triggers, the remaining three photons are in an entangled state.

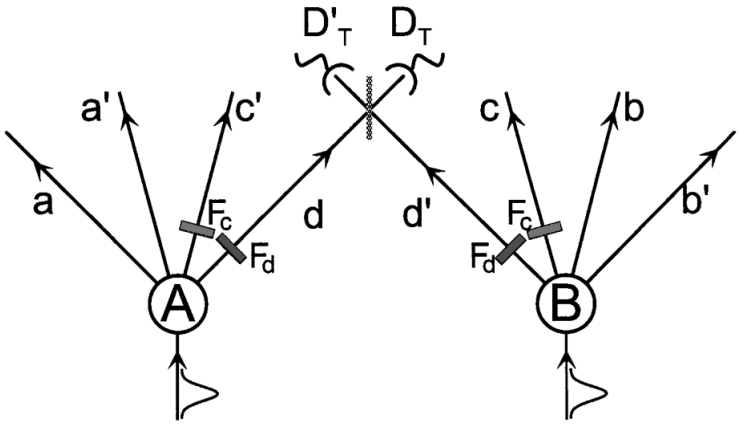

Figure 1.7: Basic scheme for GHZ state generation from [46]

The inconvenient in using this technique is that it relies on the ratio and the precision of the sources. The most used sources for the generation of two entangled photons exploit spontaneous parametric down conversion (SPDC) [12]. A well established method for the generation of GHZ state exploiting SPDC is described in [18]. They use a cascade of two SPDC set up to achieve the final state (Figure 1.8).

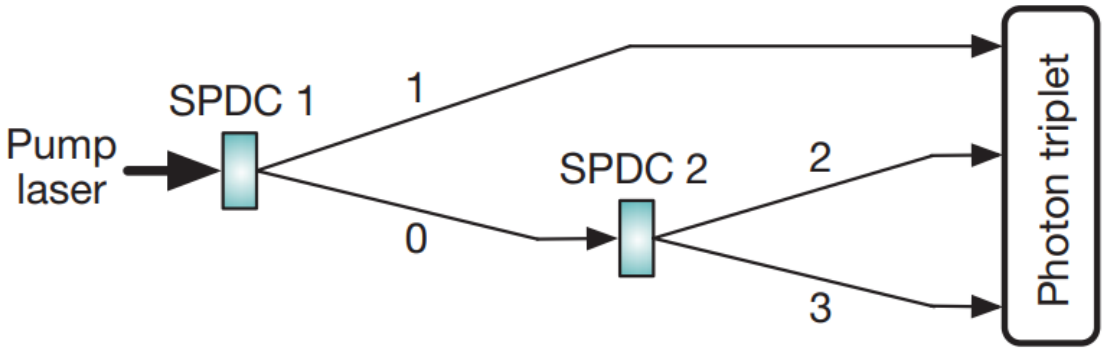

Figure 1.8: GHZ state generation exploiting cascade SPDC from [18]

The drawback of this method relying on SPDC, is that it exploits non linear effects, so high pump power is needed and the output efficiency is low.

Recent achievements in the generation of GHZ states, exploits linear optics to generate path-encoded GHZ states [46][4][23]. The generation of the state is *probabilistic*, meaning that we can be sure of having obtained the correct state only by measuring it. The problem is that this measurement makes the wavefunction collapse, thereby destroying the GHZ state. Furthermore the probability of successful generation goes as 2^{1-N}, which is exponentially reducing as the number of photons is increased. To obtain a usable state

to produce clusters, we need to be sure that we have generated a GHZ state without measuring it and this is the topic of the next section.

1.3.3. Heralded GHZ generation scheme

This last section is devoted to the most recent achievement on the generation of GHZ states: the heralded GHZ. The measurement of some photons, called heralders, in a precise state, ensures the generation of the GHZ state of three other photons, which are not subject to any measurement operation. We now present such a scheme, from [45], adapted and reported in figure 1.9. Six indistinguishable single photons are injected on the left in precise spatial modes. They pass through a series of 50/50 beam splitters and then come out on the right. If the detectors are triggered, following the heralding condition, then a GHZ state has been produced on the output, in the figure labeled as the three qubits.

The work presented in this thesis improves the schemes obtained in previous master thesis. The circuit layout and improvement points will be discussed in details in the following chapters. The final aim is to obtain a circuit for the heralded GHZ state generation, with high efficiency and also high generation rate, so it can be exploited as a starting point for a photonic quantum computer.

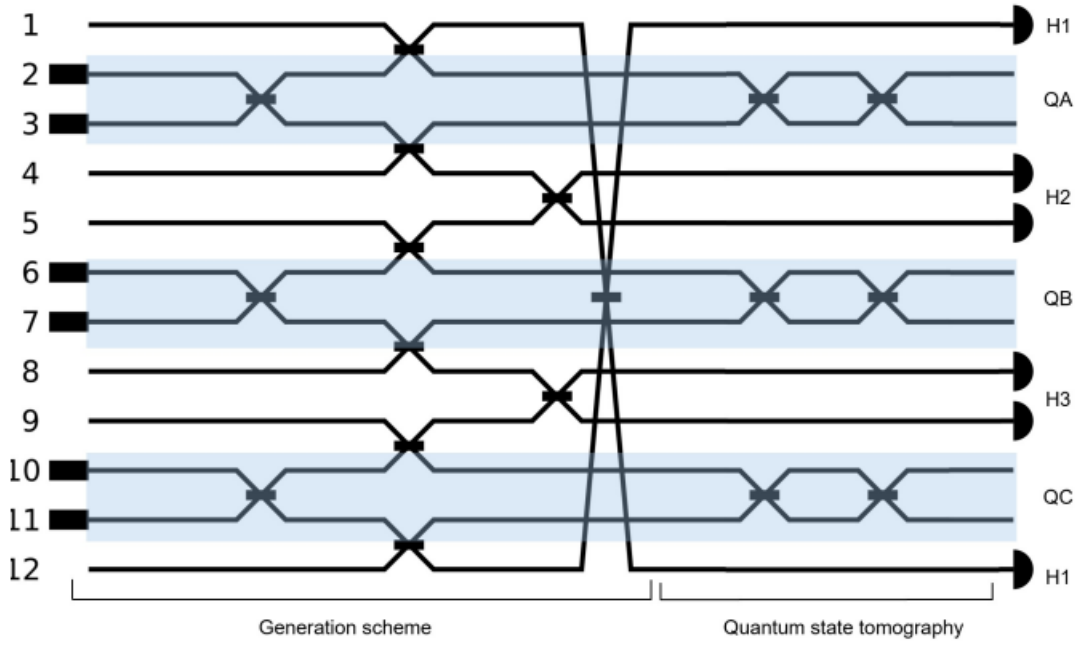

Figure 1.9: Heralded GHZ scheme, image taken from [20]. The black lines are waveguides, the black rectangles on the left are single photon sources, the half circles on the right are detectors for the heralders, the small black rectangles where the waveguides cross are 50/50 beam splitters.

1.4. Conclusions

In this chapter has been given an overview on the concepts at the basis of quantum computing. Then the focus was brought towards photonic quantum computing, alongside its strengths, one for all very low decoherence; and its weaknesses, mainly the difficulty to implement two-qubit gates, which are needed for any algorithm implementation. To solve this problem, an approach called one-way quantum computing has been proposed. This eliminates the necessity of two-qubit gates, exploiting an initial entangled cluster state. This entangled multi-photon state comprehends thousands of photons, so to build it a three-photons entangled state is needed at the very basis: the GHZ state. The purpose of this work is the implementation of a circuit for the generation of heralded GHZ states, useful as a basic building block for a photonic quantum computer.

2 | Integrated optics by Femtosecond Laser Micromachining

In this chapter will be presented the integrated optical devices needed as building blocks for our final device. Femtosecond laser micromachining technique (FLM), used to fabricate them, will be discussed in details. The phenomena occurring to induce a permanent modification of a material will be presented, from a theoretical point of view. All the relevant parameters to engineer the process will be discussed.

2.1. Optical devices

In this section the integrated optical devices exploited in this thesis work will be discussed, from a theoretical point of view. Relevant properties for the following work will be highlighted.

2.1.1. Optical waveguides

Waveguides are the basic building block of guided optics. These structures can guide the electromagnetic radiation through a well defined path.

The fundamental principle of a guiding system is total internal reflection [24]: all the radiation impinging at the interface of the two media (coming from the medium with refractive index n_1) at an angle

$$\theta_c \leq arcsin(n_2/n_1) \tag{2.1}$$

is totally reflected. The condition for the existence of this critical angle is $n_1 > n_2$. This is derived from Snell's law.

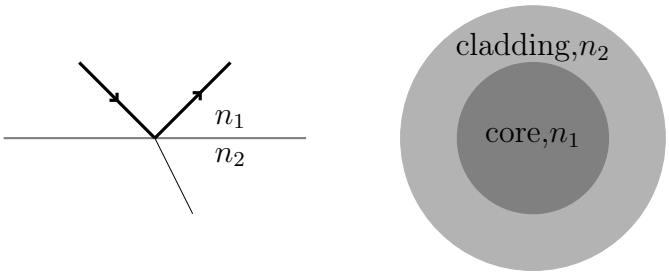

Figure 2.1: *left:* Total internal reflection and evanescent wave at the interface of two mediums; *right:* cylindrical waveguide section.

When total internal reflection happens, an evanescent wave propagates in the second medium. This evanescent wave amplitude decreases exponentially with the penetration distance in the second medium. It does not transport energy and this is why all the radiation is confined in the medium 1 with total internal reflection. However, if a third medium with refractive index greater than the second is placed at a sufficiently small distance, the evanescent wave can be coupled in this medium, before its amplitude goes to zero. The solution of the Maxwell's equations in the third medium is again a plane wave, which transports energy. This phenomenon will be crucial for the implementation of couplers.

There are many geometries that allow for guiding radiation. A direct calculation is possible, through the Maxwell equations, of the sustained modes. A mode is a distribution of the electromagnetic field which can propagate in the waveguide. For the different frequencies of the radiation, each waveguide can be monomodal or multimodal. Starting from Maxwell's equations, it can be easily derived an equation for propagating waves in a medium [39]:

$$\nabla^2\mathbf{E}(\mathbf{r},t) - \frac{n^2(\mathbf{r})}{c^2}\frac{\partial^2\mathbf{E}(\mathbf{r},t)}{\partial t^2} = 0 \tag{2.2}$$

where $\mathbf{E}$ is the electric field, n is the refractive index of the medium and c is the speed of light in vacuum. This is valid in general. Applying it to the structure of a waveguide, so with an interface between two different mediums, supplements the wave equation with boundary conditions, so that only certain distribution of fields are possible. These are exactly the modes sustained by the waveguide. For a complete derivation refers to [39]. The final result for a cylindrical waveguide, constituted by two dielectric materials, is that it can be characterized by this number:

$$V = \frac{2\pi a}{\lambda}\sqrt{n_1^2 - n_2^2} \tag{2.3}$$

where a is the radius of the waveguide and λ is wavelength of the radiation in vacuum, n_1 and n_2 are the refractive index of the core and the cladding as can be seen in Figure2.1. If $V < 2.405$ the guide is monomodal. It is valid for a simple geometry of a waveguide, but in general the number of modes sustained depends on the parameters present in this equation: the difference of the refractive indexes, the dimension of the waveguide and the wavelength of the radiation.

In the following work will be of interest to have single mode waveguides, because the power can be transferred between different modes of the waveguide and this is something we want to avoid. Most importantly couplers do not behave in a predictable way for multi-modal waveguides and we need precisely tuned couplers, as will be explained in the next section.

2.1.2. Directional couplers

Directional couplers are the other fundamental building block for our integrated circuit. They allow a power exchange between two close enough waveguides. By exploiting the evanescent wave, always present for any propagating mode in a guide. This evanescent wave can be coupled to another waveguide if it is close enough to the previous one.

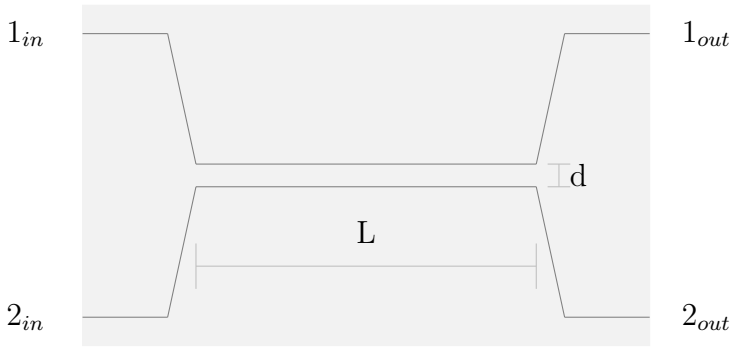

Figure 2.2: Directional coupler made with two waveguides.

The evanescent wave amplitude decays exponentially with the distance from the guide, so if two waveguides are far enough, the coupling between them is negligible. To visualize this phenomena look at Figure 2.3.

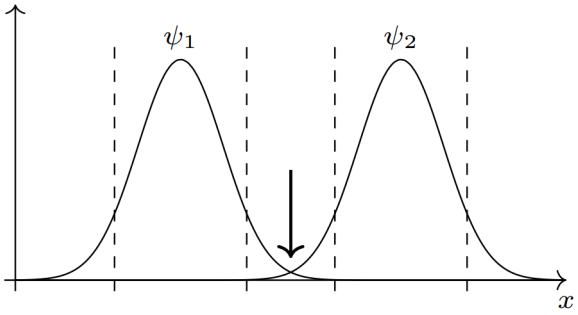

Figure 2.3: Overlapping modes of two nearby waveguides.

The exponential tails of two modes of different waveguides may overlap, this leads to an exchange of power between the two modes. A simple expression for this power exchange can be derived in the case of weakly coupling condition: when the two regions exchanging power are not too close. Moreover, considering that the two waveguides have the same refractive index, which is exactly the case for our device, the expression becomes even simpler:

$$\begin{cases} P_1(z) = cos^2(kz) \\ P_2(z) = sin^2(kz) \end{cases} \tag{2.4}$$

where P_i is the fraction of total power present in mode i and z is the coupling length (L in Figure 2.2). The plot in Figure 2.4 shows how the power splitting depends on the interaction distance.

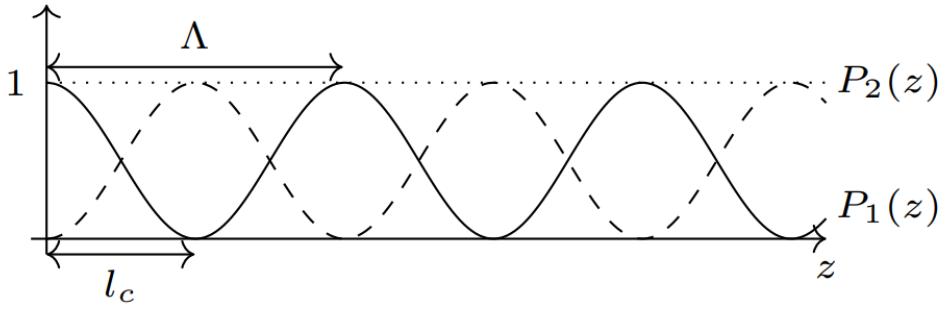

Figure 2.4: Fraction of total power present in each waveguide as a function of the coupling length.

In a physical device a directional coupler will have fixed dimensions, so an important quantity can be defined: the splittign ratio. It is defined in equation 2.5, as the fraction of power collected at the output 1 with respect to the total power at the output.

$$SR = \frac{P_1, out}{P_1, out + P_2, out} \tag{2.5}$$

The splitting ratio depends on d, L, but also on the regions where the waveguides are getting close together, so where they are at a distance higher than d, but not high enough to neglect the coupling. All of these factors have to be taken into account during the fabrication process. Here just a theoretical overview of the basic concept has been given, to give the reader the knowledge to understand the choices taken during the fabrication procedure. The practical implementation of the directional couplers will be treated in the next chapters, starting from the concepts explained here, but deepening the discussion to other relevant phenomena to be taken into account.

2.1.3. Thermal phase shifters

Thermal phase shifters [26] are able to introduce a phase shifting between two different modes (here we are referring to spatial modes, so different waveguides), exploiting the thermo-optical effect [29]. In general the refractive index of a material is dependent on the temperature of the material itself. Exploiting this dependence, it is possible to change the refractive index just by changing the temperature. The change of refractive index influences the propagation velocity of the radiation in the medium, thus modifying its phase with respect to a mode kept at a different temperature.

To perform this phase shifting accurately, only a portion of a single waveguide needs to be heated up, while the others guides remain at a different temperature. To achieve this goal a metal layer is deposited by means of lithography [30], only above the guides in which the phase shift has to be performed. Then flowing a current in this layer heats it up, by Joule effect [24]. This heat is diffused to the waveguide underneath, thus changing its refractive index in the portion affected. To achieve this result the waveguides must be vertically close to the interface where the metallic layer is deposited. Examples of a thermal phase shifter are shown in Figure 2.5 and 2.6. In the latter are visible two isolation trenches. These structures are dug into the glass substrate containing the waveguides. The conduction of heat is much lower in air than the solid substrate. They ensure thermal isolation between the region affected by the heating and the rest of the device.

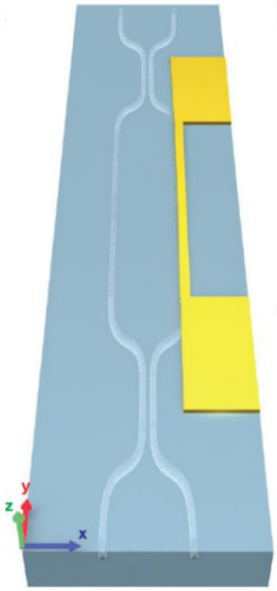

Figure 2.5: Thermal phase shifter. Metal deposited on top of the surface of a glass containing waveguides. Image taken from [8].

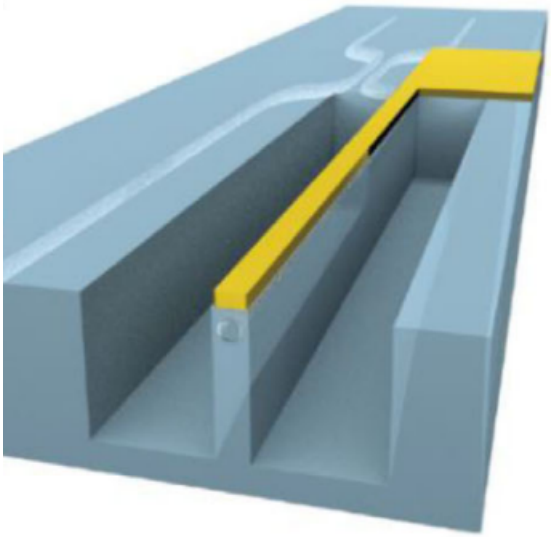

Figure 2.6: Trenches. Isolation of the region below the metal resistance from the rest of the glass. Image taken from [8].

This technology requires also work of optimization, outside of the scope of this thesis. Nevertheless, trench fabrication was based on the work of the group of Professor Osellame, in which I worked on this thesis. They optimized these devices in the last few years and keeps working to improve their thermal isolation, performance and compactness [8] [7].

2.2. Bulk modifications induced by ultrafast laser pulses

In this section Femtosecond Laser Micromachining (FLM) technique will be explained in details, both from a theoretical and a practical point of view. Starting from the general concepts and then moving to the relevant features for the specific structures employed in this work.

2.2.1. Introduction to Femtosecond Laser Micromachining

The effect of energetic IR laser pulses fired on transparent material has been studied for more than thirty years now. In particular, if the beam is focused in a sufficiently small spot and the energy is high enough, a permanent modification can be induced in the material [19]. With this modifications, a number of devices can be created: optical waveguides [27], couplers, diffraction gratings [34], lenses and microfluidic channels [28], to cite some.

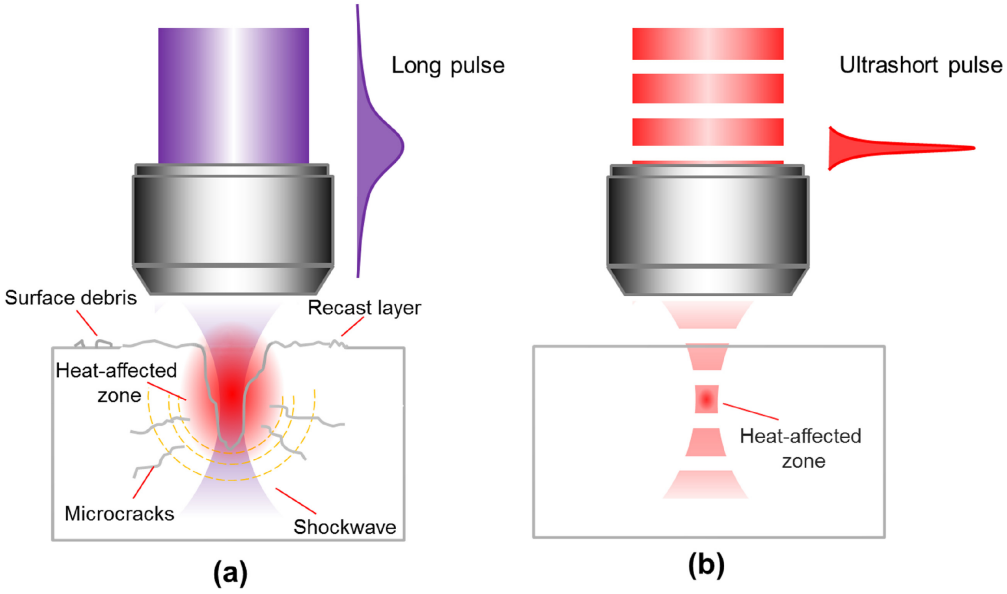

Figure 2.7: Focusing an ultrashort laser pulse in a transparent material allows for a 3D fabrication. The only part of the material affected is the focal point, leaving the rest unmodified. If a longer pulse is focused in a glass the outcome is completely different.

The very strength of this technique is the possibility to fabricate in three dimensions. The laser can be focused in any point inside a transparent material, the modification is induced only in this precise point. Exploiting slits moving with high precision, a 3D structure with any desired architecture can be obtained. Moreover, this technique avoids the need for a cleanroom environment.

To comprehend how this technique works a scheme is shown in Figure 2.8.

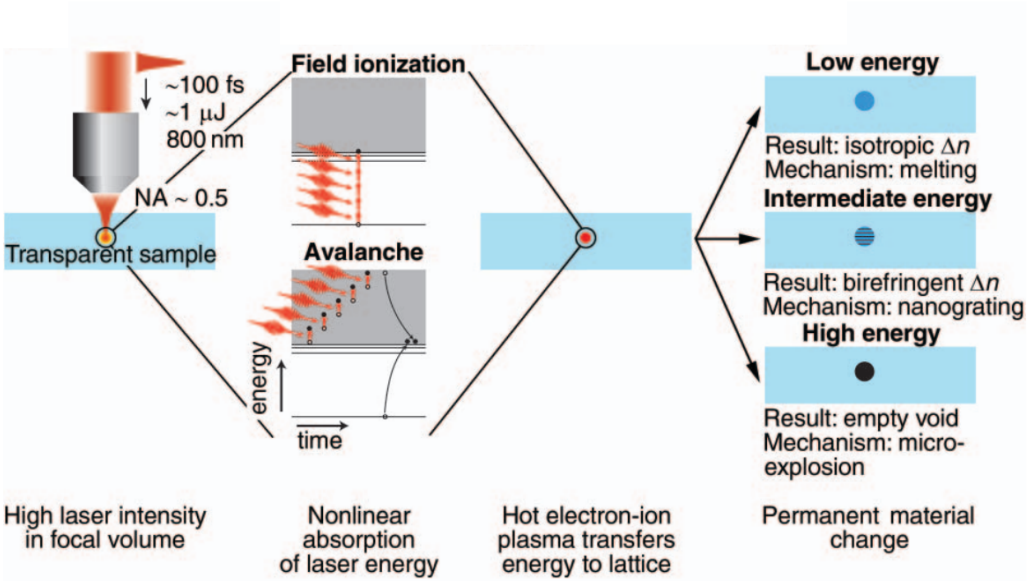

Figure 2.8: Femtosecond Laser Micromachining principles. Image taken from [19].

A femtosecond pulsed laser is focused in a transparent material. In the focal spot the intensity is very high. This leads to non linear and non-thermal phenomena [19], needed to perform this technique. With linear absorption the material will just be heated. If we keep giving energy it will break. This is schematized in Figure 2.7. The electron distribution takes a few hundred femtoseconds to a few picoseconds to reach thermal equilibrium after the irradiation. The energy transfer from electrons to the lattice (thermalization) requires tens to hundreds of picoseconds. With non-linear absorption only a small portion of the energy of the radiation is converted into heat and this leads to phenomena like field ionization and avalanche ionization. These create an electron-ion plasma, localized in the focal spot. The successive plasma recombination and energy dissipation, brings a permanent modification of the material.

The possible outcomes of this modification are of three types. They depends on many parameters of the substrate and the irradiation process. In general, keeping the other parameters fixed, the energy of the pulse induces different modifications. For low energies an isotropic change in the refractive index can be achieved, with which we can fabricate waveguides. Increasing the energy birefringence can be obtained. For even higher energies a cavity in the material can be formed, with which we can do micro and nano channels. In this work the change of refractive index is utilized to fabricate waveguides and couplers, while the possibility to form a cavity, so dig in the material, is employed to craft trenches.

2.2.2. Ultrafast pulses absorption by transparent materials

A more detailed treatment of the phenomena involved in the permanent substrate modification is required.

Thermal diffusion length: As already explained, the shorter duration of the pulses (femtoseconds) compared with the typical electron-phonon relaxation time, produces non-thermal effects, but also reduces substantially the zone of the material heated up. A diagram with the timescale of all the phenomena involved in the process is reported in Figure 2.11.

The thermal diffusion length [40] for absorption of pulses with duration higher than the electron-phonon coupling time is

$$l_d = \sqrt{\kappa\tau} \tag{2.6}$$

with κ the thermal diffusivity of the material and τ the pulse width. For femtosecond pulses, the thermal diffusion is almost negligible. The thermal diffusion length, for temperature T_{im} close to the material melting point, is given by

$$l_d = \left[\frac{128}{\pi}\right]^{1/8} \left[\frac{DC_i}{T_{im}\gamma^2 C_e^i}\right]^{1/4} \tag{2.7}$$

where D is the thermal conductivity of the material, C_i is the lattice heat capacity, $C_e^i = C_e/T_e$ (where C_e is the electron heat capacity and T_e is the electron temperature) and γ is the electron–phonon coupling constant. This corresponds to hundreds of nanometers, much smaller than the modification induced in the focal point (few micrometers).

Multi-photon absorption: With femtosecond pulses the absorption of multiple photons simultaneously, to excite a single electron, may happen. This is due to the very high concentration of photons in a very short pulse. This mechanism is depicted in Figure 2.9. Thanks to this phenomena, it is possible to fabricate in materials normally transparent to the radiation. Only in the focal point the density of photons is high enough to allow for multi-photon absorption. In the rest of the material the radiation travels without being absorbed, if the photon energy is lower than the bandgap (necessary condition to have a transparent material to a certain radiation frequency).

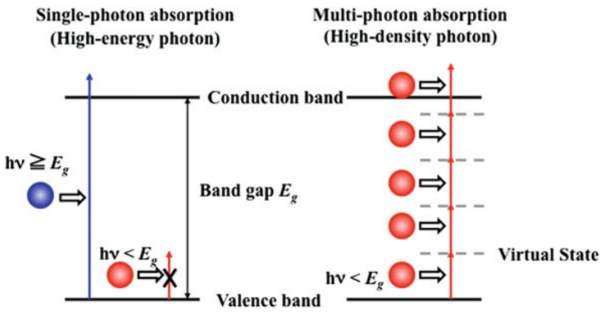

Figure 2.9: Multiphoton absorption scheme. Image taken from [40].

Tunnel ionization: This second mechanism of ionization competes with the previous one, being predominant at lower frequencies and higher powers of the laser. The electric field generated by the laser beam deforms the valence and conduction band of the material. As can be seen in Figure 2.10, the potential barrier seen by an electron is reduced on one side. This favours tunneling of electrons from the valence to the conduction band, so they can escape the molecule.

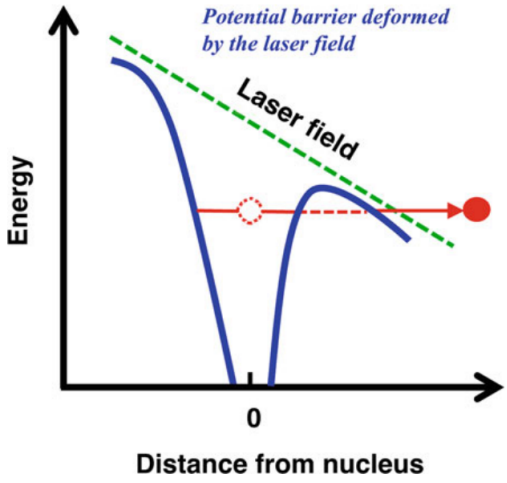

Figure 2.10: Tunnel ionization process. Image taken from [40].

Keldysh parameter: This parameter is useful to understand which mechanism of ionization is predominant. It is defined as

$$\gamma = \frac{\omega}{e}\sqrt{\frac{m_e c n \epsilon_0 E_G}{I}} \tag{2.8}$$

where ω is the laser frequency, I is the laser intensity, m_e is the electron effective mass, e is the fundamental electron charge, c is the speed of light, n is the linear refractive index of

the material, ϵ_0 is the permittivity of free space and E_G is the band gap of the material. For $\gamma \gg 1$, multi-photon absorption is predominant; for $\gamma \ll 1$, tunnel ionization is predominant. If γ is close to one both mechanisms occur. Regardless of the dominating mechanism, is thanks to these phenomena if it is possible to fabricate 3D structures in a transparent material.

Permanent structural changes: The electrons excited by both photoionization processes, continue to feel the laser field and, if it is high enough, this brings to avalanche ionization mechanism. The electrons are accelerated to high speed, enough to ionize other atoms, so that more electrons are present to be accelerated and this mechanism keeps going like an avalanche.

We end up with a plasma of ions and electrons, very localized in the focal volume. During the fabrication process is possible to see this plasma with naked eye. As this plasma recombines, dissipating energy, a modification in this zone of the material happens. This relaxation happens in time scales of picoseconds to nanoseconds. It is totally decoupled from the absorption phenomena (look at Figure 2.11). This is the relevant factor to permits structural changes with femtosecond laser pulses. The mechanisms responsible for the permanent structural changes are not fully understood, but there is a lot of experimental evidence in literature, reporting three types of modification: smooth refractive index change, birefringent refractive index change and void formation.

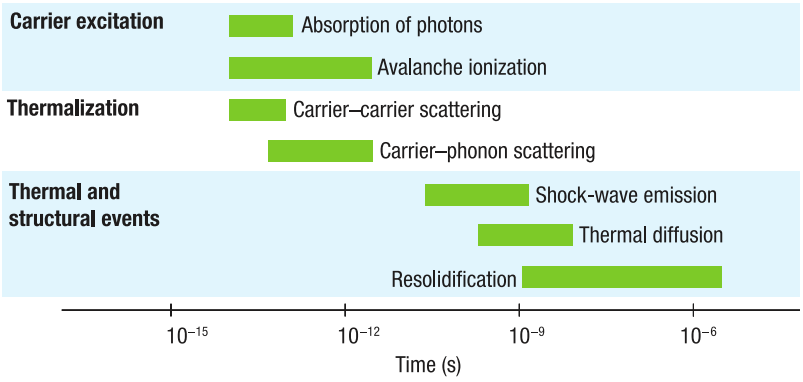

Figure 2.11: Timescale of the phenomena involved in Femtosecond laser micromachining. Image taken from [13].

2.2.3. Relevant parameters for inducing modifications on glass

There are many different parameters that influence the outcome, when femtosecond laser pulses are fired at a transparent material.

First of all, an intensity higher than a certain threshold is needed, to achieve the phenomena explained in the previous section. Again this is not precisely defined and depends on the material, but using femtosecond pulses is the only way to have such high intensity in a small volume.

Once above this threshold, different parameters come into play. For the laser source are relevant the energy, the pulse duration, the repetition rate, the wavelength, the polarization, the focal length, the scan speed. Some of this parameters enters in the Keldysh parameter defined before (Equation 2.8, so they are responsible for the prevalent ionization phenomena triggered in the material. This may influence the modification apported. The scan speed and the repetition rate of the laser define how many pulses are fired at the same spot and at which rate. If the time between two consecutive pulses is higher than the relaxation time needed by the material to go back to equilibrium, the effect of the pulses is just summed over, but they can be treated independently. If the time between the pulses is shorter than that, then we enter in a different regime called accumulation regime. A lot of heat is accumulated in the focal volume, due to the rapidly fired consecutive pulses. A graph showing this phenomena is reported in Figure 2.12. The mathematical model developed in [10] works very well in explaining this phenomena.

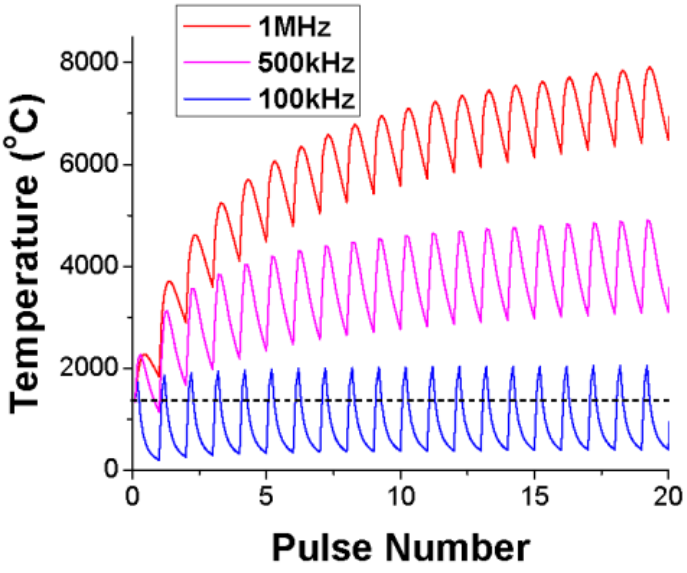

Figure 2.12: Heat accumulation dependence on repetition rate. Image taken from [10].

Another important factor is the focusing of the laser beam. A small focal point is needed to achieve in a small region an intensity beyond the threshold for the material modification. To do this microscope objectives are employed. They are able to compensate for the

aberrations present when the beam crosses the interface between two different materials. Considering the aberrations negligible it is possible to calculate the beam waist and the elongation of the focal spot [28]:

$$w_0 = \frac{M^2\lambda}{\pi NA} \tag{2.9}$$

$$z_0 = \frac{M^2 n\lambda}{\pi NA^2} \tag{2.10}$$

where where M^2 is the Gaussian beam propagation factor, NA is the numerical aperture of the focusing objective, λ is the free space wavelength and n is the refractive index of the material. So an higher NA provides a smaller and less distorted focal spot, but also increases the spherical aberrations [25]. To reduce this effect water immersion fabrication may be employed. Both the objective and the target material are immersed in water, to reduce the refractive index mismatch felt by the focused beam, being $n_{air} < n_{water} < n_{glass}$.

Other than the irradiation parameters, some properties of the substrate are relevant concerning the type of modification that will result. The bandgap of the material and its thermal conductivity are two main factor to be taken into account. The precise influence of these parameters on the outcome of the fabrication is not clearly understood right now, nonetheless this technique is widely used and studied and many great results have been obtained [40].

2.2.4. Waveguides and trenches fabrication

Let's focus on the two main structures required for the final device fabrication: waveguides and trenches.

Waveguides: To fabricate a waveguide a smooth change in the rafractive index of the material is needed. This has to be homogeneous to achieve a waveguide with low losses. To get this type of modification, the energy of the pulses must be just above the threshold to have a modification in the material. So in general for waveguides fabrication is used an high repetition rate for the pulses, which implies lower energy for the single pulse.

The mechanism believed to be the responsible for this kind of modification is a rapid solidification, after the melting of the material in the focal spot. The focal spot is at an higher temperature with respect to the rest of the modified volume. It cools down, starting from the edges in contact with the rest of the material at a lower temperature. We are in the bulk, so it is not possible to expand this volume. This implies that the central part cools down under pressure. This may result in an higher density in this spot. This in fused silica implies an increase of the refractive index, exactly what is needed to have a waveguide embedded in a glass material. Other factors may play a role, like color

centers [19] and the shockwave generated by the laser focusing [37].

An annealing [17] step is needed, for certain substrates, to obtain a waveguide with low losses. The material is heated up, below its melting point. There are different regimes for a glass material depending on its temperature [1]. For every material the annealing process has a different recipe, but the concept behind it is the same. Going above the strain temperature allows to reduce all the mechanical stress accumulated during the fabrication [42], by rearranging the damaged parts. This has been demonstrated to improve the guiding structure, can be even obtained a single mode waveguide from an initial multi mode one [1].

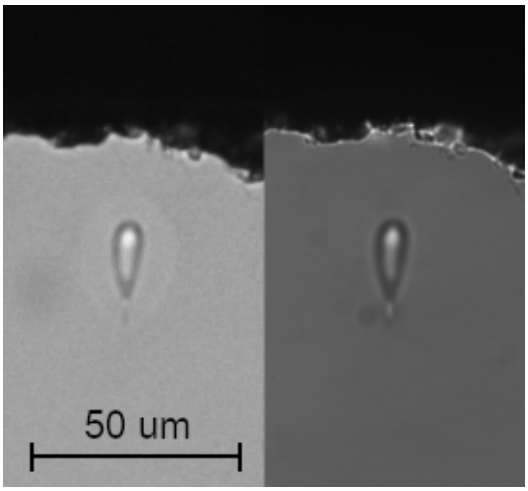

Figure 2.13: Section of a waveguide before (left) and after (right) the annealing procedure.

Trenches: These structures are of fundamental importance to thermally isolate different parts of the device. To fabricate them high energy per pulse is needed, to induce a modification of the void type. Usually the repetition rate is much lower than the one used for waveguide fabrication. The peak intensity of the pulse is so high that produces a pressure greater than the material's Young's modulus [28]. This creates a shockwave after the electrons have transferred their energy to the ions. The shockwave leaves behind a less dense or hollow core. Repeating this for many steps leads to digging a trench in the material. The actual parameters and optimizations performed are discussed in the next chapters.

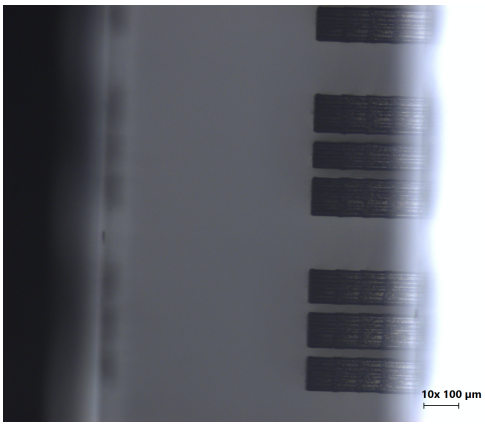

Figure 2.14: Trenches in Borofloat, side view at the edge of the sample.

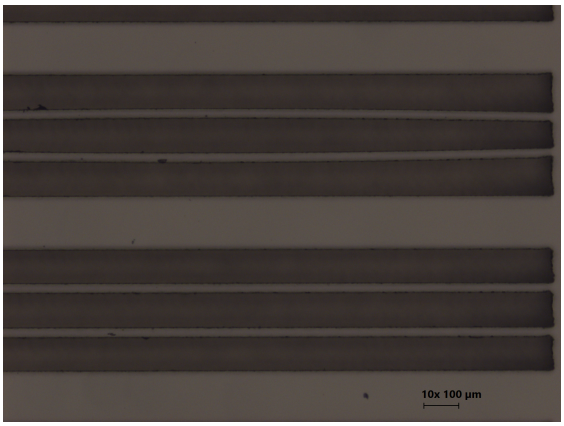

Figure 2.15: Trenches in Borofloat, top view of the sample.

2.3. Conclusions

Waveguides, couplers and thermal phase shifters are the building blocks exploited to achieve the goal of this work. Their theoretical functioning has been discussed in this chapter. To realize them the technique of femtosecond laser micromachining has been used. It provides many advantages, on the top of them 3D fabrication and no need for clean room or other particular environment setup, just a suitable laser to focus on a glass material. The physical phenomena occurring after the focusing of femtosecond laser pulses in a material have been described. They lead to permanent modification in the focal spot. Tuning different parameters of the irradiation and choosing the correct material, low losses photonic chips can be realized.

3 | Methods for fabrication and characterization of photonic chips

In this chapter will be described the fabrication and the characterization setups utilized to realize femtosecond laser writing of waveguides.

3.1. Fabrication setup

In this section the fabrication setup is presented. A general overview is given, followed by the several components. The software used for programming the positioning system is presented. The last paragraph is devoted to the two glass substrates utilized: Borofloat and EagleXG and also the post fabrication procedures a sample undergoes before the characterization: annealing and polishing.

3.1.1. Laser source and focusing system

A schematic of the fabrication set up is shown in Figure 3.1. On the left we have the laser source. The beam immediately passes through two half-wave plates and a polarizer. These are needed to attenuate the beam. One of the two half-wave plates is electronically controlled by the same system that controls the motion of the sample. By putting a powermeter right before the sample, is possible to tune precisely the power we are going to use to fabricate. After the polarizer, the beam undergoes a series of reflections, at a number of dielectrical mirrors, also out of plane. These guide the beam up to the objective, above the sample. The objective focuses the beam on the sample. A CCD camera is placed behind one of the mirrors, to capture the back reflection of the beam on the facets of the sample (the mirrors do not reflect 100% of the radiation, the small amount transmitted is enough for the camera to capture it). In this way we are able to recognize if the beam is focused on one of the facets of the sample. The last component

is the motion system, on which the sample is mounted.

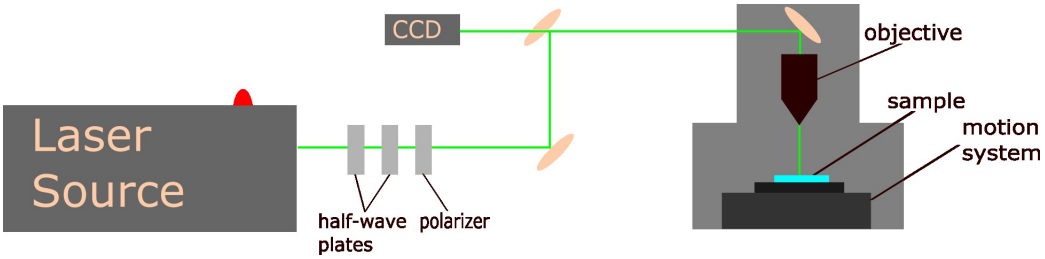

Figure 3.1: Schematic fabrication setup. At the exit of the laser source (which could be either PHAROS or CARBIDE) there are two half-wave plates and a polarizer to attenuate the beam. Then the beam undergo reflections at different mirrors, to arrive at the objective and be focused on the sample. The back reflection is captured by a CCD camera. The sample is placed on a holder, mounted on the slits of the motion system.

Now that the comprehensive system has been described, let's focus on the main components, which deserves a deeper explanation. In this work two laser sources have been used, while the fabrication line is the same for both of them.

Pharos:

This is the laser used to achieve the final result of this thesis work. This laser is from the Pharos lasers series, by the company Light Conversion. It is a diode pumped Yb^{3+}:KGd$(WO_4)_2$ laser oscillator, controlled in temperature by a water cooling system. The pump diode excite a crystal rod of KGd$(WO_4)_2$, which is doped by 5% Yb in concentration. This material emits at a wavelength of 1030nm. The pulsed regime is achieved by mode locking [41]. The chirped pulse amplification technique [35] is employed, through beam amplification and successive compression, to achieve pulses with duration $<$190fs up to 10ps, with single pulse energy up to 1mJ. The repetition rate can be controlled via a Pockels cell and a pulse picker and increased up to 1MHz. The maximum average output power is 10W. All these parameters can be tuned directly from the control program of the laser itself. This laser incorporates also a system for the second harmonic generation, at a wavelength of 513nm. The last mechanism worth mentioning is the electrically controlled laser shutter, which ensures a fast response during the fabrication process.

Carbide:

This laser is from the same company of the previous one, but belongs to the Carbide series. It is again a diode pumped Yb mode-locked laser. This one is water cooled too.

The emitted wavelength is also 1030nm. The maximum output power is 5W, less than that of Pharos. The pulse duration ranges from <190fs to 20ps. The maximum energy for each pulse is 100μJ. The repetition rate can go up to 1MHz. This laser was used to fabricate mainly in Borofloat (one of the glass substrate discussed later on in this chapter), during a period when Pharos was under maintenance. Having characteristics very close to each other, it should be possible to find analogous fabrication windows with both lasers.

3.1.2. 3D sample motion

To fabricate 3D structure in a glass by focusing laser pulses on it, a precise motion system is required. All the fabrication setup presented before is fixed up to the the objective. The objective can move only along the vertical direction, while the sample moves in the horizontal plane. The glass substrate is attached to an holder with air cured polymeric coating. This allows to keep the sample stable, but it is easy to remove after the fabrication is complete, with a bit of acetone. The holder can be filled with water, which is a requirement for the fabrication of isolation trenches. It is mounted to a two axis tilt platform, to tune manually the tilt of the sample. This structure is anchored on the motion system *Aerotech FIBER-Glide 3D*. This system employs compressed air and a feedback mechanism to achieve 2nm resolution, maximum velocity of 200mm/s and maximum acceleration of 20m/s^2.

3.1.3. *femto*

To control the motion stages described in the previous section, a program has to be loaded on the software controlling the system. The program has to be written in G-code. This is a programming language with specific features to control the 3D movement of the system. *femto* is a Python open source library, created by Riccardo Albiero. It has been created to simplify the code writing part of the fabrication. With a simple Python script it is possible to implement a variety of structures, building each waveguide piece by piece. Then the G-code is automatically generated. The structure is plotted in 2D or 3D, which allows an actual visualization of the final result, before the fabrication. It is very useful to spot errors in the code and to understand the most adeguate writing strategy for the device in hand and also to discuss the design of the fabrication with other colleagues.

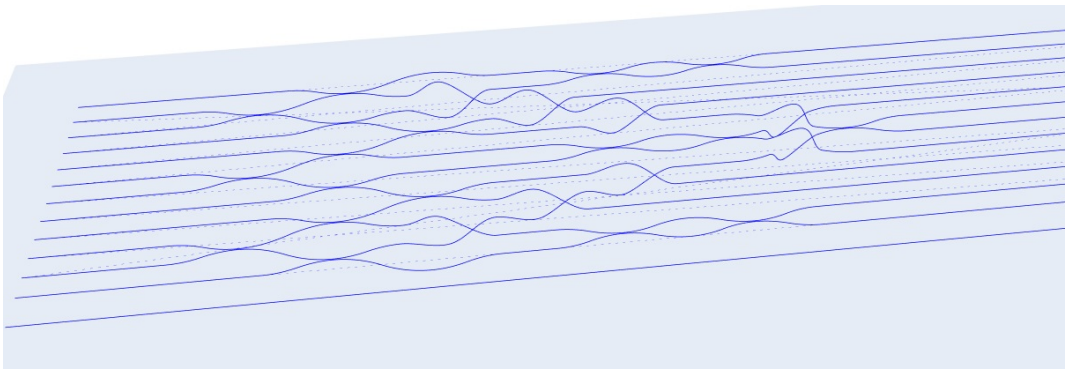

Figure 3.2: Example of a 3D plot of different waveguides generated with *femto*

There are a lot of other features that make *femto* so useful, but I will linger only on one more: the trenches fabrication. Usually many lines of G-code are required to fabricate a trench, it is an iterative process with a lot of steps. Precise coordinates have to be inserted in the code to obtain the wanted final result. With *femto* this becomes much easier. With just one line of Phyton code is possible to generate multiple trenches, just by giving as inputs two dimensions to delimit an area. The library automatically digs the trenches around the waveguides structures present in the zone, leaving them untouched. The fabrication of the trenches is performed on a sample containing a photonic circuit already characterized. For this reason it is needed to align the sample as it was aligned during the circuit fabrication. The black crosses visible in Figure 3.4 fulfill this purpose. They are laser ablation done on the bottom face of the glass and are visible with the CCD camera. Moving between different crosses along the sample it is possible to understand if the alignment is correct and otherwise adjust it.

```
# internal phase trenches
d = br/2 - dh(L_trench/2) + int_maxw - 0.014
x_pos = [ ref_x_Jack + 2*dx_s + arm_length/2 ]
y_pos = [ (y0_global + 0*pitch_GHZ-d, y0_global + 1*pitch_GHZ+d),
          (y0_global + 5*pitch_GHZ-d, y0_global + 6*pitch_GHZ+d),
          (y0_global + 10*pitch_GHZ-d, y0_global + 11*pitch_GHZ+d) ]

for xc, (ymin, ymax) in list(product(x_pos, y_pos)):
    col = TrenchColumn(x_center=xc, y_min=ymin, y_max=ymax,
                       length=L_trench, **PARAMETERS_TC)
    col.dig_from_waveguide(fabb[GHZ_to_trench-1])
    tcols.append(col)
```

Figure 3.3: Example of Phyton code employing *femto*, to realize the trenches in Figure 3.4

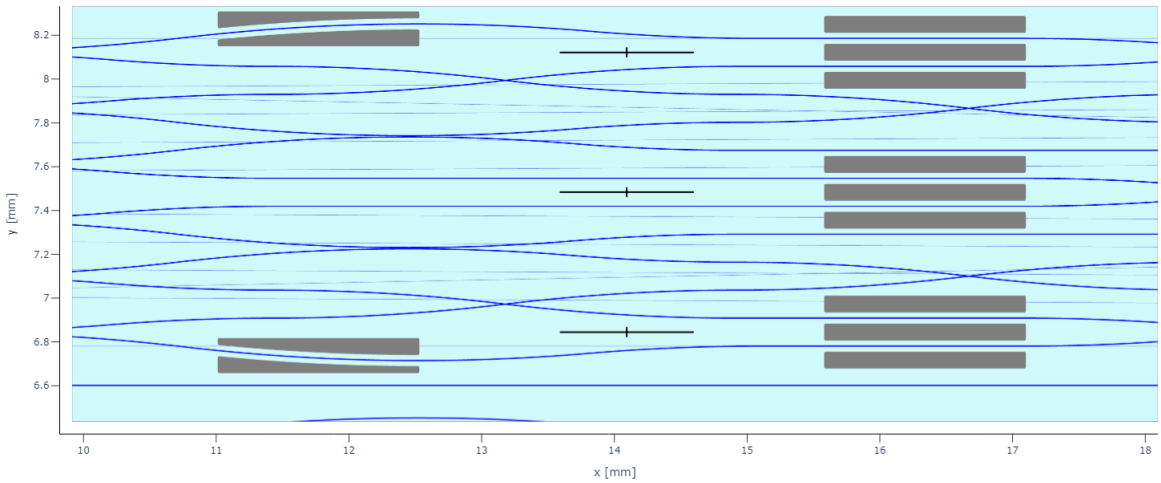

Figure 3.4: 2D plot generated with *femto*. The blue lines are the waveguides, the black crosses are laser ablation, while the grey filled structures are the trenches. The latter are obtained from the command "dig.from.waveguide". It can be seen clearly in the left ones, that the profile of the guides has been followed, keeping a fixed distance from them to avoid any risk of interruption.

3.1.4. Glass substrates and post fabrication processes

Two different types of glass have been used during this work: Borofloat and EagleXG. They are both borosilicate glasses, provided by different companies, which produce them according to the specification needed, with controlled thickness. The main characteristic for both is the high transparency to IR radiation, which is fundamental for FLM with the lasers we used.

The procedure of fabrication is the same for both glasses. Before the actual fabrication, the sample needs to be cleaned manually with optical tissue and acetone, to remove any piece of dirt that may distort the laser beam; this issue is more relevant if the fabrication occurs closer to the upper surface of the substrate. For Borofloat the fabrication was carried out in air. On the other hand for EagleXG the fabrication was carried out in water immersion, meaning that the sample and the objective are both immersed in deionized water.

After the fabrication, the sample undergoes an annealing procedure. This is different for the two glasses, because they have different strain points and annealing points. The annealing procedure reaches 750°C for EagleXG, a temperature higher than the 590°C for Borofloat. Anyway the annealing procedure follows the same principle. The sample is placed in a oven, it starts to heat up above the annealing temperature, but below the

melting temperature, it remains there for few minutes and then is cooled down very slowly below the strain point. After that a faster cooling is performed back to room temperature. A very relevant particular regarding the annealing procedure is the expansion of the sample. We have completely different behaviours for Borofloat with respect to EagleXG. The first one shrinks after the annealing while the latter expands. Here we talk about expansion of 1μm/cm, which seems negligible, but in the final steps, when the pigtailing with a fiber array is required, the distances between each mode of the device has to match perfectly the ones of the fiber array. So in any fabrication this expansion/contraction has to be taken into account, to obtain a correct device after the annealing.

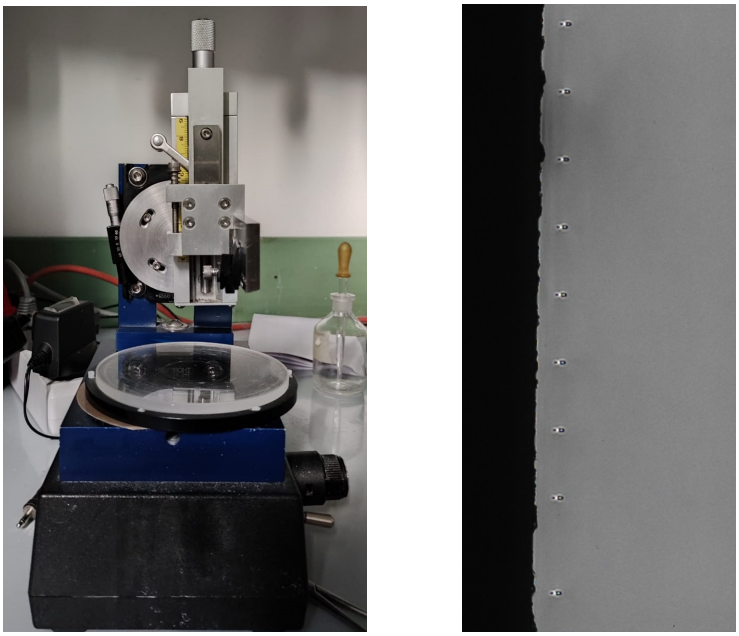

Figure 3.5: On the left the automatic polisher, on the right a microscope image of a sample after the annealing and the polishing. The sections of some waveguides are visible, while in the facet of the sample there is no visible roughness nor scratches.

After the annealing the sample is almost ready to be characterized, just more one step is necessary. The input and output facets of the sample have to be polished. This minimize the losses by scattering, ensuring a good coupling with the optical system. To do so a FLex Waveguide Polisher by KrellTech is employed, an image is reported if Figure 3.5. A succession of sand paper discs is used, starting from a roughness of 30μm to a final roughness of 0.3μm. The polishing also removes the tapering from the sample. It is a layer with many defects and stress. The tapering is due to the entrance of the laser beam in the sample. It is clearly visible by a microscope inspection. Tapering extends up to $\approx 500\mu$m from the input/output and it is responsible for the increasing coupling loss, so

it has to be removed. The first sand paper disc is enough to remove this layer.

3.2. Inspection and characterization methods

In this section the waveguide characterization setup will be described. First of all a microscopic observation is performed to ensure that the fabrication has been carried out correctly. Then optical measurements of the structures are performed, to obtain their transmission, the splitting ratios of the directional couplers and the mode profiles.

3.2.1. Microscope observation

The first control done on a chip after the fabrication, is the visual inspection through a micrscope (Nikon ME600). Even with the minimum magnification (4x) the structures fabricated are visible. The slight refractive index change of the waveguides, is enough to make them observable.

Figure 3.6: Microscope image of some waveguides taken with a PixeLINK B871 camera. On the bottom the two waveguides getting close to each other, without touching, form a directional coupler. Just above this, two waveguides cross out of plane forming a bridge.

Usually with this microscope check it is possible to control if the fabrication has been carried out as expected. Also is possible to see if any waveguide is interrupted. A clear break is visible if, for example, a grain of dust was deposited on the surface of the sample.

It may interrupt the waveguide. The last check done with the microscope regards the trenches. It is possible, pouring a drop of acetone and looking at it while evaporating, to check if the trenches are empty or if some residuals of glass is still in them.

3.2.2. Optical characterization set-up

After the microscope inspection, the optical characterization of the device is carried out. With the setup in Figure 3.7 is possible to measure the insertion losses and the mode profiles of the waveguides.

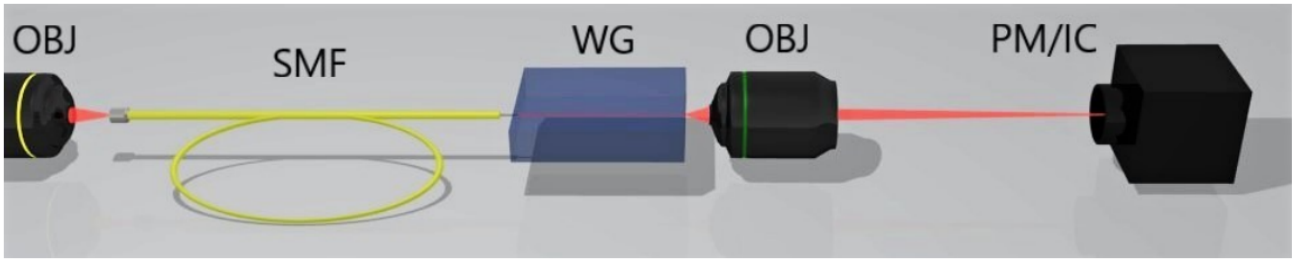

Figure 3.7: Scheme of the characterization setup

A laser diode, controlled both in current and temperature, to set the output power and the output wavelength, is coupled, after some reflection on metallic mirrors, through an objective (OBJ), into a single mode fiber (SMF). This fiber is a Thorlabs single-mode fiber 780HP, it is single mode at 925nm, which is the wavelength of our interest and also the wavelength of the laser diode. The optical fiber is then coupled to the waveguides of the device (WG), bringing it very close to the input facet of this one. Behind the chip is placed another objective, to collect the radiation that passes through and to focus it on a powermeter (Ophir NovaII), to measure the power.

To be able to precisely align the fiber and the objective to each waveguide, a system of two 6-axis computer controlled hexapods (H-811.F2 by PI-Physik Instrumente) is employed, as shown in Figure 3.8. The fiber, secured to the fiber navette, and the objective, mounted on a holder, are placed on a Hexapod. The Hexapod is a platform which can move along the x,y and z directions and rotate around each of these three axis, having a total of six degree of freedom. A precision of 100nm allows to precisely align with any waveguide and compensate any unwanted tilt carried out during the fabrication. Other than the Hexapods a CCD camera is mounted on the top of the set-up, to capture a live image of the tip of the fiber and the sample and help during the coupling procedure. The central object is the sample holder. This is controlled by software too and can move along the vertical and horizontal axis. It has also three rotational degree of freedom controlled

manually, to adjust the tilt of the sample after it is mounted.

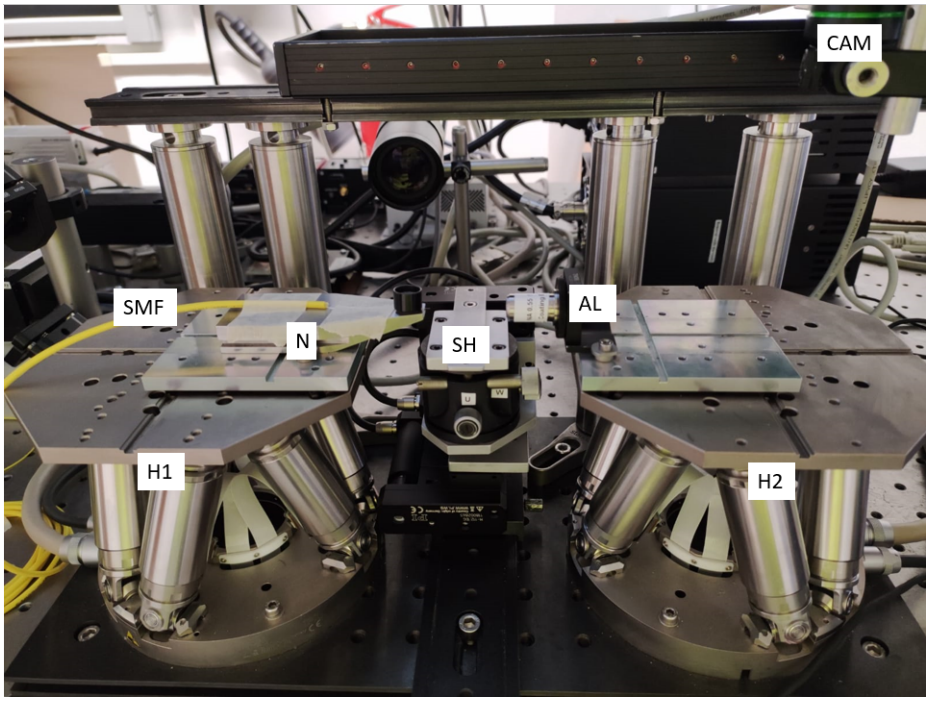

Figure 3.8: Characterization setup with two hexapods H1 and H2. On the left one the single mode fiber (SMF) on its navette (N) is mounted. On the right one is placed the aspherical lens used as objective (AL). In the middle the sample holder (SH), the structure above it is to move the CCD camera (CAM).

A similar setup has been used to characterize the mean field mode profile of the waveguides. This is useful to calculate the coupling losses, due to the superposition of the incoming fiber mode with the one of the waveguide, but also to understand if the waveguides are single or multi modal. To do so, the powermeter placed on the right of Figure 3.7 is replaced with a Emdund Optics EO-1312M CCD sensor, sensitive to the infrared.

The near field distribution of waveguide and fiber are imaged by the same system and the images are saved. Then through a Python program the two profiles are compared, so as to get information about their superposition. To check if the waveguide is single mode, it is sufficient to move the fiber at the input and control that no modes different than the fundamental Gaussian one are excited and so captured by the camera.

3.2.3. Device losses measurement

To perform a measurement of the transmission of a waveguide, it is necessary to measure first the power without the guide as a reference. To do so the sample is removed and the

fiber is coupled directly to the objective, as can be seen in Figure 3.8. In this way all the losses of the system are taken in to account, except for the ones of the device and a negligible contribution of airbound propagation loss. So when a measure with the sample in place is performed, the difference (in a logarithmic scale) between the power measured and the reference that we have, accounts only for the losses due to the chip.

With the kind of measurement just described, the insertion losses of a waveguide can be obtained

$$IL_{dB} = -10log_{10}\left(\frac{P_{out}}{P_{in}}\right) \tag{3.1}$$

where P_{out} is the power measured at the output of the sample, while P_{in} is the power measured at the input of the sample, which corresponds to the reference taken without the sample. This gives the insertion losses in dacibel (dB). The insertion losses are the result of different contributions, that will now be described.

Fresnel's losses:

These are due to the back reflection, caused by the mismatch of the refractive index of two different materials, in this case air and glass. It can be calculated from the Fresnel coefficients, assuming normal incidence, resulting in the equation below

$$FL_{dB} = -10log_{10}\left(\frac{(1-R)P_{in}}{P_{in}}\right) = -10log_{10}\left(1-\left(\frac{n_1-n_2}{n_1+n_2}\right)^2\right) \tag{3.2}$$

where R is the reflectivity, that can be expressed through the refractive indexes of the two materials n_1 and n_2. These losses have to be taken into account twice, because we have this interface both at the input and at the output of the glass.

Coupling losses:

These are due to the mismatch between the fiber and the waveguide modes. As said before, to estimate these losses it is necessary to capture the images of the modes so as to retrieve the electric field distribution of both. Then to calculate the coupling losses one uses the following equation

$$CL_{dB} = -10log_{10}\left(\frac{|\int\int E_{wg}(x,y)E_{of}(x,y)dxdy|^2}{\int\int |E_{wg}(x,y)|^2dxdy \int\int |E_{of}(x,y)|^2dxdy}\right) \tag{3.3}$$

where E_{wg} is the electric field distribution of the waveguide, while E_{of} is the electric field distribution of the optical fiber. For the calculations a discrete counterpart of 3.3 is used, since the retrieved modes are 2D array of light intensity.

Propagation losses:

The propagation losses are due to the propagation on a straight portion of a waveguide and are expressed in dB/cm. They are given by

$$PL_{dB/cm} = -\frac{10}{l} log_{10}\left(\frac{P(l)}{P(0)}\right) \tag{3.4}$$

where P(l) is the power after a propagation for a distance l, while $P(0)$ is the power at the beginning of the guide. These losses do not account for the other contributions described in this section, so to estimate them a procedure called cut-back is employed. It is a destructive procedure, where the insertion losses of a straight waveguide are measured, then a portion of it is cut. The losses are measured again and this procedure is repeated a few times. At the end an estimate of the propagation losses can be given, considering the reduction of the measured losses with respect to the length of the portion of the waveguide which has been cut.

In the end the insertion losses are due to three different terms for the straight waveguides

$$IL_{dB} = 2FL_{dB} + CL_{dB} + l \cdot PL_{dB/cm} \tag{3.5}$$

Curved waveguides have, in general, an excess loss with respect to straight waveguides at the same length. Usually we are interested in the propagation losses. The procedure of cut-back explained before takes a long time and it is also destructive. An easier way to calculate the propagation losses, is to measure the insertion losses of a straight waveguide and then subtract from it the coupling losses, calculated in the way previously explained, and the Fresnel losses, calculated by using the refractive indexes of air and glass.

3.2.4. Directional couplers characterization

In this last section are discussed some properties of the directional couplers, relevant for their implementation in the photonic circuit.

Splitting ratio dependence on the coupling distance:

Starting from the coupling modes theory, already discussed in Chapter 2, the solution for a mode propagating in the z direction, for two close waveguides, is the linear combination of the two modes of the single waveguides:

$$\Psi(x,y,z) = A_1(z)\psi_1(x,y)e^{-i\beta_1 z} + A_2(z)\psi_2(x,y)e^{-i\beta_2 z} \tag{3.6}$$

where $\psi_1(x,y)$ and $\psi_2(x,y)$ are the modes of the single waveguides, β_1 and β_2 are the two wavevectors and A_1, A_2 are two amplitude coefficients depending on z. This satisfies the Helmoltz equation, in a medium with a refractive index n(x,y), so with a spatial dependence, like in the case of a coupler where we have two regions with an higher refractive index (the waveguides) inside a lower refractive index region (the rest of the glass). By substituting in the Helmoltz equation and neglecting the second order terms, like $\frac{\partial^2 A_i}{\partial z^2}$, with respect to the first order ones, we get this system of equation:

$$\frac{d\mathbf{A}}{dz} = -iM(z)\mathbf{A}(z) \tag{3.7}$$

where M(z) is the following (2x2) matrix:

$$M(z) = \begin{pmatrix} k_{11}(z) & k_{12}(z)e^{2i\delta z} \\ k_{21}(z)e^{-2i\delta z} & k_{22}(z) \end{pmatrix} \tag{3.8}$$

each matrix element is of the type:

$$k_{il} = \frac{k_0^2}{2\beta_i} \frac{\int\int \psi_l^2 \Delta n_l^2 \psi_i dxdy}{\int\int \psi_i \psi_i^* dxdy} \tag{3.9}$$

they are overlapping integrals of the modes of the waveguides, in the regions where the refractive index changes. The diagonal elements can be neglected because they refers to the single waveguide, so no refractive index change. We are left with the two antidiagonal elements, which in the case of FLM are identical, because the two waveguides that form the coupler are identical. Also the δ terms, related to the mismatch of the wavevectors are zero for equal waveguides. The final matrix is:

$$M(z) = \begin{pmatrix} 0 & k(z) \\ k(z) & 0 \end{pmatrix} \tag{3.10}$$

Now the system of equation 3.7 can be solved if the coefficients k(z) are know. They are

overlap integrals, as stated before, and can be modelled with an exponential along z.

$$k(z) = \alpha e^{-\gamma d(z)} \tag{3.11}$$

d(z) accounts for the geometry of the coupler, α and γ are the parameters we have to find. In all the regions where the waveguides are close enough, the exchange of power can happen. The most relevant term is the γ coefficient, it is the one that regulates the power exchange. We are able to numerically find the values for these coefficients, that best fit the measured data from the couplers fabrication with different coupling distances, knowing the shape of the function that rules the power exchange in a coupler. With this procedure we are then capable of calculating the coupling distance value that gives a coupler with 50% splitting ratio.

Differential losses characterization:

If the two waveguides making a coupler have different insertion losses, the splitting ratios measured entering from different inputs of the coupler may be different. To check that this phenomena is not present, is performed a measure of the power at each output entering from both inputs. Referring to Figure 2.2 four powers are obtained: $P_{1,1}$, $P_{1,2}$, $P_{2,1}$ and $P_{2,2}$; the labels indicate the input and the output channels. The parameter D can be defined as

$$D = \sqrt{\frac{P_{1,1} * P_{2,1}}{P_{1,2} * P_{2,2}}} \tag{3.12}$$

In this way we account for the different losses of the waveguides. If this parameter value result close to 1, the differential losses are negligible. If its value is far from 1 the coupler suffers of relevant differential losses. Acceptable values are in the range 0.96 to 1.04.

3.3. Conclusions

A description of the fabrication setup and characterization setup has been given. The fabrication procedure relies on a program written in G-code, which controls both the shutter of the laser and the movement of the sample. To simplify the writing and visualization of these programs the Phyton library *femto* has been used. The characterization has been done exploiting two hexapods and their high precision and stability, with the set-up of Figure 3.7. With the same set up, putting a powermeter or a CCD camera at the end, is

possible to characterize respectively the losses of a waveguide, or its mode profiles.

4 | Fabrication of an integrated heralded GHZ factory

This chapter presents the whole process, of successive fabrications and characterizations, which led to the integrated photonic circuit for the generation of heralded GHZ states. In the first section the implemented design of the device is discussed. Then, going in chronological order, the developed work will be presented: initially with Borofloat glass and then with EagleXG.

4.1. Final device design

Before discussing all the experimental process to achieve the goal of this thesis work, the design of the final device that we have adopted will be discussed. As already mentioned in the first chapter, the design is adapted from [4]. The actual design of the fabricated device is reported in Figure 4.1. In the initial part the state is generated, then a tomography is carried out through Mach-Zehnder interferometry. A more complete discussion, about the physics behind these, is presented in the next chapter.

The relevant points I want to highlight here are two. First, the device must have low losses, to produce the GHZ states with the highest possible rate. To reduce the losses, we want the device as short as possible; so all the directional couplers have coupling length equal to zero. Second, the out of plane bending of some guides. A plot to visualize that is reported in Figure 4.2. To implement this device some of the waveguides have to cross over some others, to make the directional coupler 11 in Figure 4.1. For this purpose, the best option is to make the waveguides of the two modes forming the coupler bend out of plane in one direction and the guides they cross bend in the opposite direction. This is needed to avoid unwanted cross-talk between the modes. Moreover there is a trade-off between the radius of curvature and the length of the waveguide. For shorter radii the guide becomes shorter, but the bending loss increases. For longer radii we obtain a longer device, with higher propagation losses, but lower bending losses. An optimization is required to find the best compromise between these two quantities.

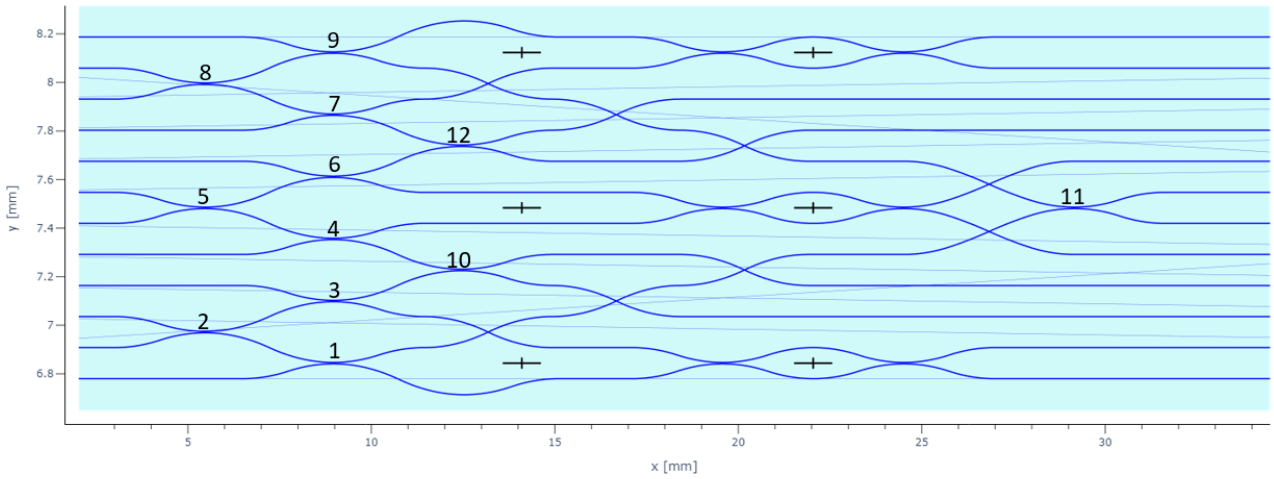

Figure 4.1: 2D Schematic of the final device, generated with *femto*. The directional couplers are labeled from 1 to 12.

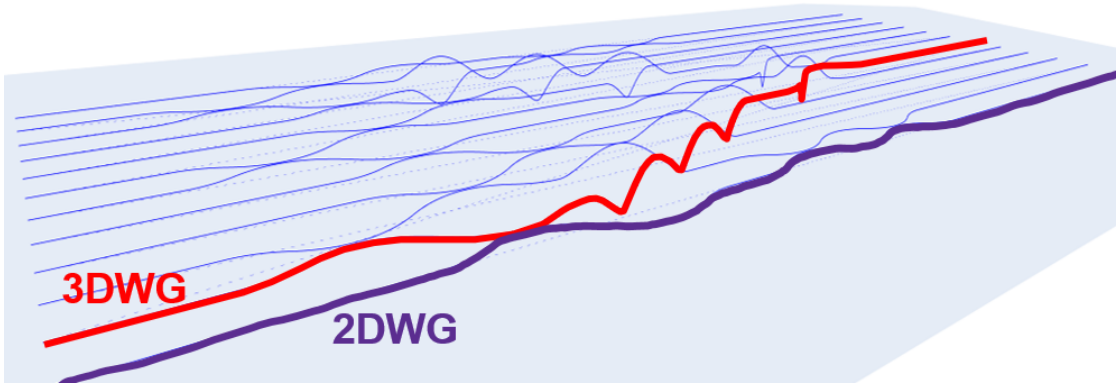

Figure 4.2: 3D plot of the final device. A waveguide bending in plane and one bending out of plane are highlighted.

The one presented here will be the design of the final device, but it is not the only one we tried. In particular the topology of the waveguides that bend out of plane, the most criticals, has been changed few times to try to reduce their losses. In the end we were able to reduce the length of the device to 3.3cm. To get to this result a lot of optimization was needed. All the procedures and decisions that led to this are discussed in the next sections.

4.2. Waveguide optimizations in Borofloat

At the beginning of this thesis, the candidate glass substrate, on which the heralded GHZ state generation device should have been fabricated, was Borofloat. This choice

was motivated by recent work of our group, suggesting higher transmission with respect to EagleXG, the other glass substrate considered as an option. So the work began with Borofloat. The experimental procedure followed is described in the next sections. It starts with the search for a suitable waveguide at 925nm.

4.2.1. Waveguide Optimization

a. Initial optimization with Pharos

For a couple of weeks, at the very beginning of my thesis, the laser devoted to the fabrication procedure was Pharos. The first step was to find a waveguide with low losses and single mode operation at 925nm. This particular wavelength is not a random choice. This device is in cooperation with another research group, which have developed a single photon source, based on quantum dots, with high repetition rate; which can be suitable for the generation of GHZ states, if combined with the integrated chip fabricated in this work. The wavelength of the photon they are generating is exactly 925nm.

The first fabrication was a series of straight waveguides, where each one had a different set of fabrication parameters. In particular the parameters we controlled are: the average power of the laser, the writing velocity, the number of scan for a single guide and the writing depth in the glass. As already explained in the second chapter about femtosecond laser micromachining, these parameters influence the outcome of the fabrication. We do not know precisely how the variation of one of this influence the outcome, but in general depositing more energy in the same area of the glass produces a stronger modification.

An example is reported in Figure 4.3. The waveguides are seen from the input. They exhibit an elongated shape, similar to a drop; the laser was focused on the visible bright spot, where is the actual guide. Looking at the images the effect of the different writing parameters is clearly visible: increasing the power, the number of scan, keeping fixed the other parameters, generates a larger waveguide. On the contrary, increasing the velocity produces a smaller waveguide. In this fabrication the depth was kept constant for all the guides, in fact they are all aligned. Having larger waveguides in general means lower propagation losses, but also the possibility of having a multimode waveguide. For the final device, single-mode guides are required, to ensure a predictable behaviour of the directional couplers, since different modes of a waveguide can exchange power between them.

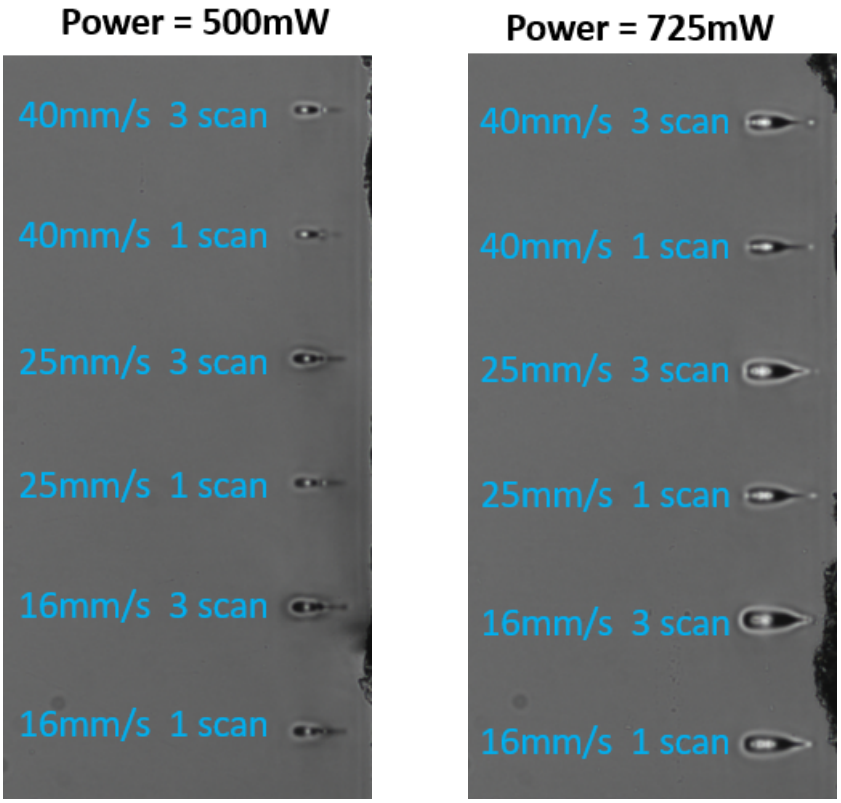

Figure 4.3: Microscope images of two groups of waveguides. The images are taken with the same magnification. The waveguides were fabricated with different powers, writing velocities and number of scans.

After having fabricated a set of waveguides and controlled on the microscope if some of them are visibly damaged, the sample was characterized. Before measuring the losses of the waveguides, near field modes inspection was done, with the goal of understanding if they are single or multimodal. After having coupled the fiber with a guide, so visualizing an image on the camera, the optical fiber is moved in the vertical and horizontal directions to try to excite modes higher than the fundamental. If only the fundamental mode is visible the waveguide can be considered monomodal.

Unfortunately, after just a couple of weeks from the beginning of my work, a fault in the compressor made Pharos unavailable for the following two months. A different laser came into play: Carbide. The characteristics of the two lasers are similar, as already discussed in chapter 3; nevertheless a writing parameters reoptimization had to take place. We were trying to find a waveguide, which requires a modification of the material just a bit above the threshold, which has to be single mode, again a condition that requires a fine tune of the parameters.

In the last fabrication with Pharos a mesh with the following parameters has been done:

- Depth = from 850μm to 870μm
- Power = from 600mW to 700mW
- Velocity = 25mm/s
- Scan = 1
- Radius = from 30mm to 60mm

The data obtained with this fabrication will not be reported. Comparing them with the one with only straight waveguides we were able to gather some useful information. First of all the depth of writing. Borofloat is very sensible to this parameter. We found a very tight window for the optimal depth. Slightly less generated only multi-modal or very high losses waveguides. Even diminishing the power below 500mW does not help, we go below the modification threshold. Going deeper than this results in a different problem. The samples we had were thin, their thickness was around 900μm. Moreover they were not perfectly flat, but had relevant bending on both sides. So a higher depth may result in writing out of the sample. Another important information was the radius of curvature. A radius lower than 40mm led to higher losses. Surprisingly even higher radii led to slightly higher losses. These are characteristics of the glass, which will not change with other laser sources.

b. Waveguide optimization with Carbide

With the information obtained with Pharos, a first optimization of the waveguide has been done with Carbide. We did not fabricate only straight waveguides, but also a guide equal to the second mode of the final chip (3DWG in Figure 4.2). This mode is the one that bends four times out of plane, so we expect it to be the one with higher losses. We are trying to optimize a waveguide with this particular form, the other will have for sure lower losses. We tried again different numbers of scans: 1 and 3. The powers used ranged from 500mW to 800mW, with steps of 37.5mW. The writing velocities were 16 mm/s, 25mm/s and 40mm/s. This made a total of 54 straight waveguides plus 54 bent waveguides. The sample length was 5cm.

The steps from the fabrication to the characterization were the same as with Pharos. It is sufficient to check the straight waveguides modes. If they are SM, so are the bent ones. If they are multi-modal, it is possible that the higher modes have higher losses in curvature, so that they are not visible in the bent guides, but they remain nonetheless

multi-modal. For powers below 575mW the propagation in the waveguide was very low. For powers higher than 650mW all the guides were multi-modal. Between these power we have a window for our waveguide. In the following figures I have reported the data for all the measured waveguides of this fabrication. In Figure 4.4b are reported the measured insertion losses in dB, for the SM straight waveguides. All the combination of parameters which are not present, generated other multi-modal waveguides.

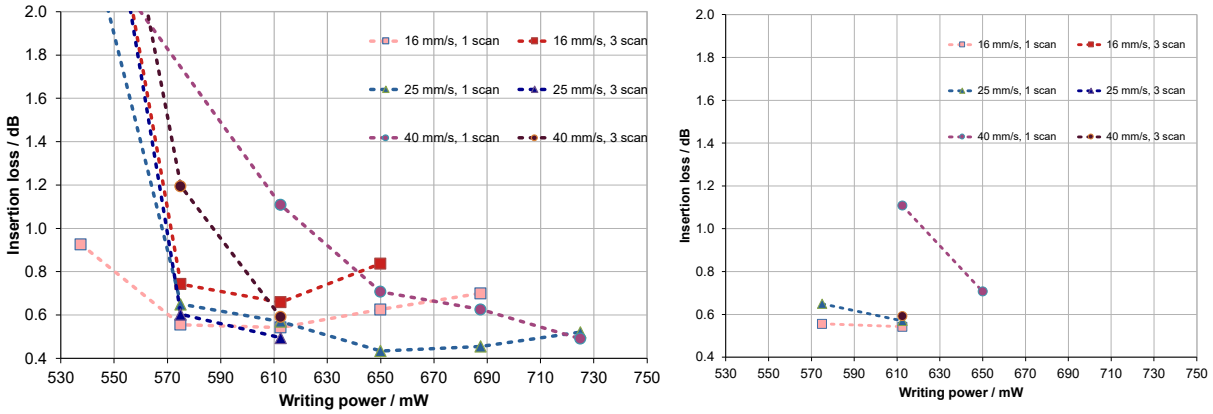

(a) All the measured straight waveguides. (b) Single mode straight waveguides.

Figure 4.4: Straight wavegudies from the first optimization with Carbide.

Only few waveguides of the whole fabrication were SM. The one with the lowest insertion losses is at 612.5mW, 16mm/s and 1 scan: only 0.54 dB. Before choosing this guide we have to check also the bent waveguides. Their losses are reported in Figure 4.5.

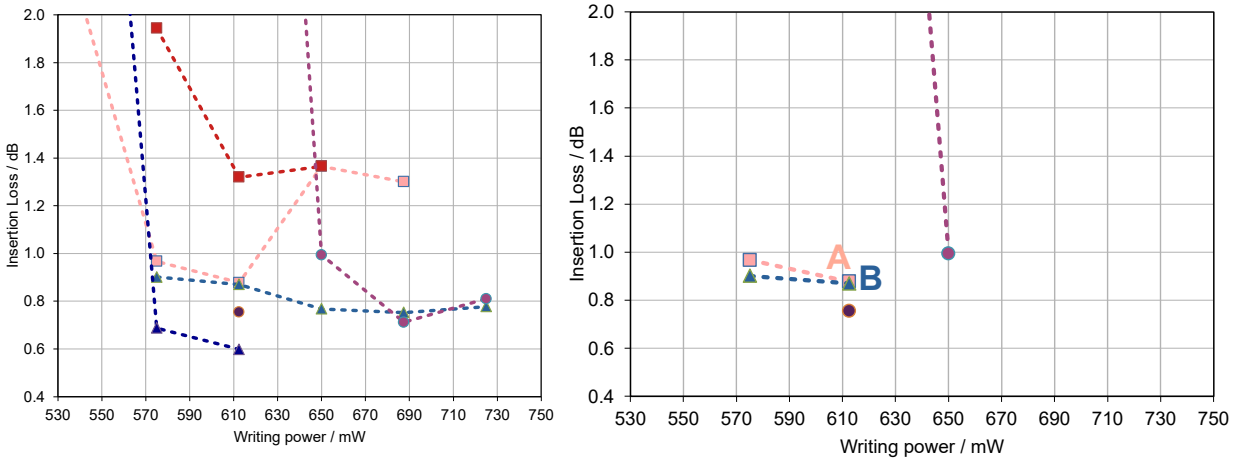

(a) All the measured 3D bent waveguides. (b) Single mode 3D bent waveguides.

Figure 4.5: 3D bent waveguides from the first optimization with Carbide.

From these data, the best bent waveguide is at 612.5mW, 40mm/s and 3 scan. We decided to pick two set of parameters for the next fabrication: 40mm/s, 3 scan, 612.5mW and 25mm/s, 1 scan, 612.5mW. The first set corresponds to the bent waveguide with the lowest losses, which is what we were looking for. The second corresponds to the second best bent waveguide (labeled as A and B in Figure 4.5b). We chose to give it a try because the losses, for 25mm/s and 1 scan, seemed quite stable even changing the power (with the same parameter at 575mW, the losses are almost the same). We decided to go on with the parameter we have chosen, but in the future it is possible to explore other possibility for fabrication, maybe at 16mm/s and 1 scan.

4.2.2. Directional couplers optimization

Now that the parameters for the waveguide have been chosen, the next step is the fabrication of couplers. For the final device a coupler with a splitting ratio of 50% is needed. We want this coupler to have zero coupling length, to make the device as compact as possible. So being the parameters of the fabrication fixed, to find the 50/50 coupler we can only act on the coupling distance. What has been done is a fabrication of 13 couplers, with coupling distances from 4μm to 10μm, with steps of 500nm. Furthermore, some straight waveguides and 3D bent waveguides have been fabricated in the same sample, to compare them with the previous fabrication and test the reproducibility. The data are presented Figure 4.6 and in Table 4.1.

In the scheme reported in Figure 3.7, the laser is coupled directly to the optical fiber. In this, and other characterizations, between the objective and the fiber, a 90/10 coupler has been added. This device splits the incoming radiation: 90% on the red path and 10% on the blue path. The red is then connected to the optical fiber and the rest of the set-up is the same. The blue is connected to a powermeter and acts as a reference. When the measure without the sample is taken, to obtain the power at the input of the sample, also the power measured by the powermeter at the blue is noted. If some instability on the power output of the laser are present, we have a reference also of the blue power without the sample. So we can compensate all the values that we gather by multiplying by the ratio between the reference P_{blue} and the P_{blue} at the moment of the measure. There are changes of few μW between the different measures, but they corresponds to tens of μW for the red path of the 90/10 coupler. This method should ensure an higher precision on the measured losses, but there is a problematic phenomena. It is possible to have some back reflected radiation, from the input face of the sample back into the fiber and the 90/10 coupler. This may increase P_{blue}, without an actual increase of P_{red}. The back reflection is caused by the difference of the refractive indexes between air and glass. It can

be reduced significantly with a correct coupling of the fiber with the waveguide. Between them an equal reflectivity Fabry-Perrot cavity is formed, so in theory 100% transmission can be achieved. We have no way to understand if this is the case. Nevertheless, even if we collect some back reflection, increasing P_{blue}, we can only overestimate the losses. This is not a critical error, in the worst case our device is better than what we have measured.

This characterization is about directional couplers. To measure the splitting ratio, which is what we are interested in, it is necessary to measure the output power of both exits of the coupler (bar and cross) entering from the same input. The set-up with the hexapods comes in handy. When coupled to the input, it is possible to move just the objective collecting the output radiation, by a distance equal to the pitch between the guides, in the direction of the other arm of the coupler. This ensures that the collected radiation is focused in the same spot as the previous arm. So there is no need to move the powermeter and these measurement can be done very quickly.

The coupling distances and all the discussed powers measured, are reported in Figures 4.6. In the Graphs 4.6a and 4.6b are reported the insertion losses, calculated considering the sum of P_{bar} and P_{cross} as the output power.

Another relevant point regarding the couplers, which needs a further discussion, is the order of fabrication. All the waveguides of the final device will be fabricated from mode 1 to mode 12. In this way all the couplers are made in the same way: first the lower arm and then the upper arm. This ensures that the couplers are all equal. The modification due to the fabrication of the lower arm, influences the material in the zone where the upper arm will be fabricated. Changing this order may change the output of the fabrication. For this reason the waveguides need to be fabricated always with the same order. To do so, the 3D bent ones must bend one upward and one downward. The mode 2 has to go below all the others, while mode 11 has to go above. This is because the changing of the refractive index induced by the fabrication influences the following fabrications, if the laser beam pass through these zones. So we must avoid to fabricate passing through an already modified zone. For this reason we have two different 3D bent waveguides to optimize, one up and one down. Being Borofloat very sensible to the depth, this may result in different losses for the two, this needs to be checked.

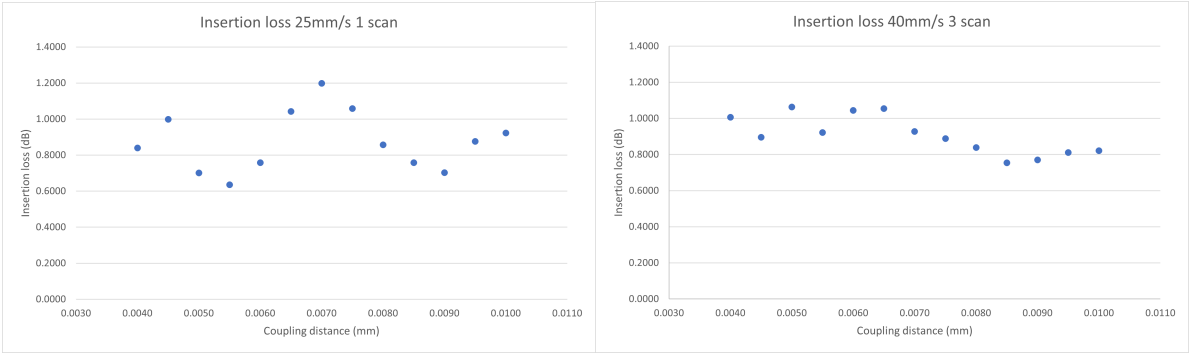

(a) Insertion loss, 612.5mW 25mm/s 1 scan

(b) Insertion loss, 612.5mW 40mm/s 3 scan

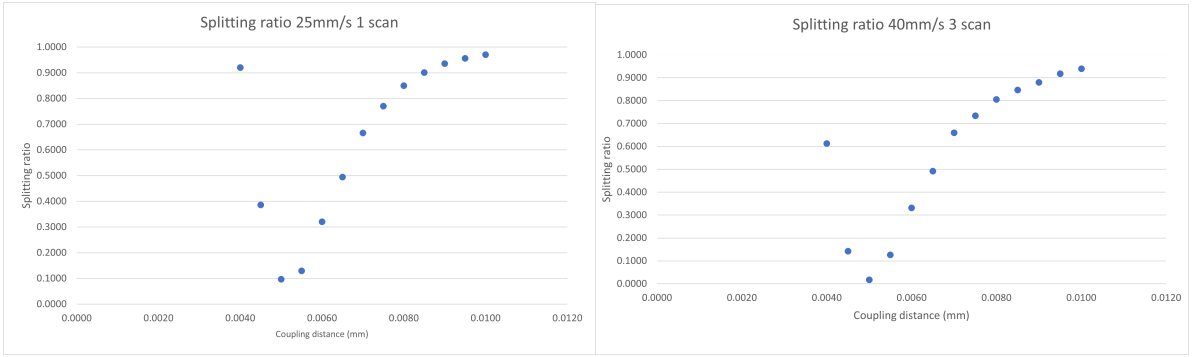

(c) Splitting ratio, 612.5mW 25mm/s 1 scan

(d) Splitting ratio, 612.5mW 40mm/s 3 scan

Figure 4.6: Plot of the insertion losses and splitting ratios, gathered from the coupler fabrication with two different sets of parameters.

Now all the choices and procedures applied should be clear, so we can analyze the data gathered from the characterization of the two series of couplers, with the two sets of parameters chosen as good candidate for the final device, discussed from the previous fabrication. In Graph 4.6a the insertion loss values are more spread with respect to Graph 4.6b, but they are all around 1dB. In the Graphs 4.6c and 4.6d is shown the splitting ratio as function of the coupling distance. These data allow us to numerically find the function determining the splitting ratio as a function of the coupling distance.

From these data, both sets of parameters seems good candidate for the final device, but comparing the insertion losses of the 3D bent waveguides in this fabrication, there is a clear winner. The data are reported in Table 4.1.

Waveguide type	Parameters	Insertion losses
SW	612.5mW 25mm/s 1 scan	0.69dB
3D down	612.5mW 25mm/s 1 scan	1.01dB
3D up	612.5mW 25mm/s 1 scan	0.97dB
SW	612.5mW 40mm/s 3 scan	0.66dB
3D down	612.5mW 40mm/s 3 scan	1.44dB
3D up	612.5mW 40mm/s 3 scan	1.16dB

Table 4.1: Measured insertion losses of different waveguides fabricated to check reproducibility. SW = straight waveguide, 3D down = 3D bent downwards waveguide, 3D up = 3D bent upwards waveguide.

The data shows that the best parameters are 25mm/s, 1 scan. The losses measured for this fabrication are higher than the ones of the first optimization of the guides, even for the parameters that now we have chosen for the final device. This is a first sign of problems with the reproducibility of the results with Borofloat glass. The measured losses are still low for a sample of 5cm length, but having this difference in the result between two consecutive fabrication is not a good sign. Nonetheless, we have a candidate set of parameters for the final device.

In order to estimate d_{50}, the coupling distance at which the splitting ratio is equal to 50%, we implemented the method described in Chapter 3 section 3.2.4. In Figure 4.7 is reported the outcome of this procedure, applied to the results obtained in the previous fabrication of couplers.

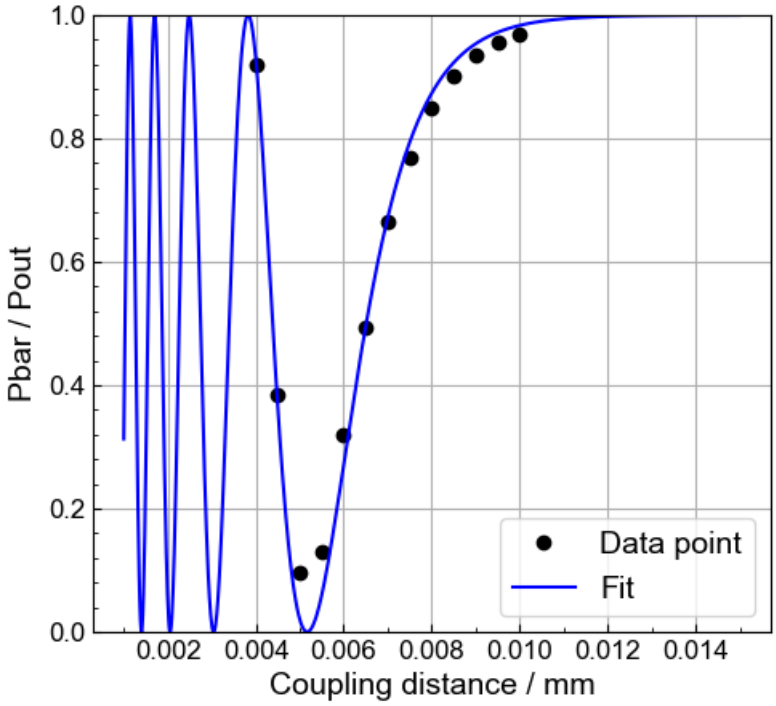

Figure 4.7: Measured values of couplers splitting ratios, fitted to find the coupling distance of the 50/50 coupler. The black dots are the experimental values, the blue line is the calculated function.

As can be seen in the plot, for small coupling distances the function oscillates very fast, meaning that several power transfers are possible on account of the high coupling coefficient. Going towards higher coupling distances the oscillations become smoother, until a threshold value is reached, when there is no more coupling. When this happens all the power is collected at the *bar* output. The gathered data are exactly on this part of the curve, where the slope of the final oscillation is much less steep than the others. We chose the d_{50} in this part of the curve, because here we are more tolerant to deviation from the optimum value. Interpolating the fitting function, we calculated the coupling distances for splitting ratio tolerances of 5% (Table 4.2).

Splitting ratio	Coupling distance (mm)
45:55	0.00639
50:50	0.00651
55:45	0.00664

Table 4.2: Calculated coupling distances for the respective splitting ratio.

The values of the coupling distances for splitting ratio different from the 50/50 are needed for the fabrication of the complete device, that will be discussed in the next section.

4.3. Complete device in Borofloat

Now that all the parameters for the complete device are decided, we can proceed with the fabrication. On a single piece of glass will be fabricated 5 devices, each one with a different coupling distance. This is done to account for some splitting ratio variability: we fabricate 5 devices with coupling distances corresponding to splitting ratios from 45/55 to 55/45 in the previous fabrication. The chip length of the complete device is 5cm and the width is 15mm.

We performed the fabrication with these parameters and obtained the complete devices. From the microscope inspection, they were not interrupted, so we proceed with the optical characterization. The gathered data were significantly different from what we expected. The losses were much higher than the ones measured during the initial optimization, for all the five devices. I will report the data of some modes of one of them, which has couplers very close to 50/50 splitting ratio (this part of the procedure worked correctly). They are reported in Figure 4.8. To measure the insertion losses of a mode of the device, the optical fiber is coupled to the input of this mode. Then the output power at each of the twelve outputs is measured. Exploiting again the hexapod it is possible to move the objective by a distance equal to the pitch between the modes and measure the power at each output keeping the setup fixed.

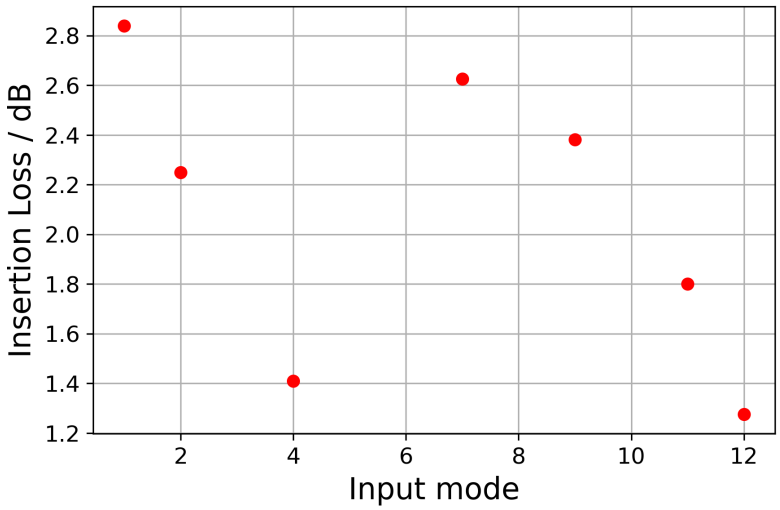

Figure 4.8: Insertion loss of some modes of a complete device from the first fabrication with Borofloat.

Based on the previous fabrications we expected insertion losses of 1.1dB, even considering the modes with more bending, which corresponds to the ones with the higher losses. The measured ones are actually much higher, for some modes even 2.8dB. These results highlight the low reproducibility of Borofloat. We had some good waveguides at the beginning, but in this fabrication it seemed that we have completely different ones. Even the best ones measured have losses higher than what we expected. This is a problem seen repeatedly when working with Borofloat. It is a very sensible glass, high precision is required in the writing depth and also in the power of the laser pulses. The Carbide laser did not help about this second point. It is more unstable than Pharos, the pulse duration had to be controlled, and adjusted manually if needed, before each fabrication. Its variable condition may have influenced the outcome of the complete device fabrication.

4.3.1. Consideration about writing depth

In all the fabrications performed we had to measure depth from the top facet going down, to be as precise as possible. The objective we used compensates the spherical aberrations, but we do not work with it in the correction point. The recipe used to found waveguides with low losses worked with this layout. This may be the cause of the high sensitivity to the depth.

A study of the writing depth was performed, testing also different powers and number of scans. The results are reported in Figure 4.9.

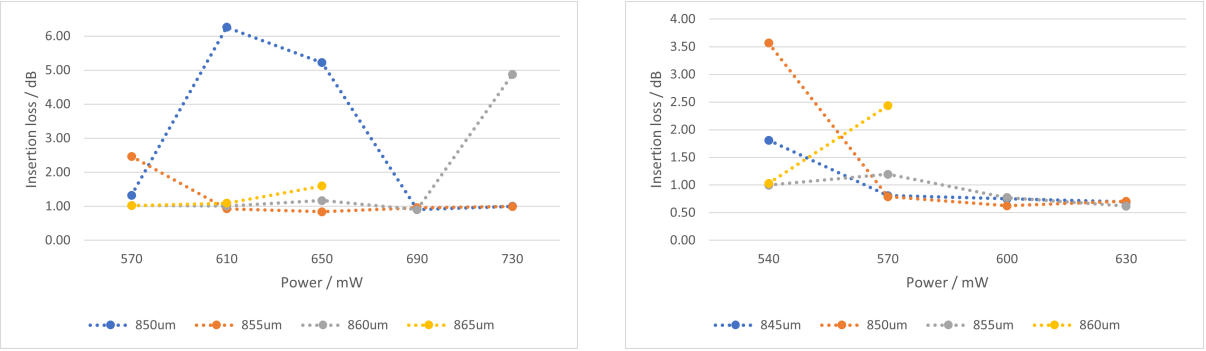

(a) Insertion loss, 1 scan, mesh of powers and depths.

(b) Insertion loss, 3 scans, mesh of powers and depths.

Figure 4.9: Insertion losses of the straight waveguides fabricated to study the depth sensitivity of Borofloat.

The above graphs show the insertion losses of all the waveguides fabricated. Most of them result in multimode waveguides. For the group fabricated with 1 scan only the two

lowest powers resulted in single mode waveguides. For the group with 3 scans only the lowest power produced a single mode waveguide. An exception is made by the highest depth for both group (the yellow series): all the waveguide shown are single mode. This highlights the sensitivity of Borofloat to the depth, a change of few micrometers resulted in the appearance of higher modes. Exploring higher depths may be a solution, but the thickness of our samples was an obstacle for this. Nevertheless keeping fixed the power and increasing the depth produced similar losses in this fabrication. For this reason we repeated the fabrication of the complete device, to understand if the higher losses measured in the previous one had some explaination.

With this second fabrication we noticed a repeating pattern: the higher losses where present in the modes propagating along waveguides with higher average depth (i.e. closer to the bottom surface). This makes sense, because Borofloat is very sensitive to the writing depth, so going down may end up in higher losses. This may have happened also because we were working with samples thinner than expected, so when moving close to the bottom surface refractive phenomena could have reduced the effective fabrication power. We measured the samples before using them to fabricate, but even the best ones had thickness of 900μm, with a bending in the horizontal direction of 15μm. This makes the fabrication very difficult. A possible solution was to compensate the depth of the whole fabrication, to follow the bending of the sample. In the end we never tried this procedure, it would have required a lot of time to implement a code capable to perform such fabrication. In the future maybe this procedure could be tested for some fabrications in Borofloat.

4.3.2. Solution for the depth sensitivity and Mantis design

Based on the obtained result we tried to change the design of the circuit, making both of the 3D bent waveguides go upward. This should reduce the losses of these guides, because going upward should not influence negatively the propagation in the guide. Multimode operations we do not expect to be a problem in the bent waveguides, an higher order mode could be lost in curvature. At the output we will have a single mode guide, so even if in the higher portion different modes are excited and some power have been exchanged between them, bending back down force the return to a single mode.

The actual problem we had to face, with the new layout, regarded the directional couplers. Fabricating the guides with this design, forced a different order of fabrication. As previously explained, we cannot fabricate passing through a portion of the glass where we already fabricated, because the change of the refractive index distort the passing beam.

So the second mode had to be fabricated after all the guides that will stand below it. This result in some directional couplers fabricated in the opposite way with respect to the other ones: before the upper arm and then the lower arm. This may result in different splitting ratio, so we made a preliminary fabrication of only couplers to test this. The results are reported in Figure 4.10.

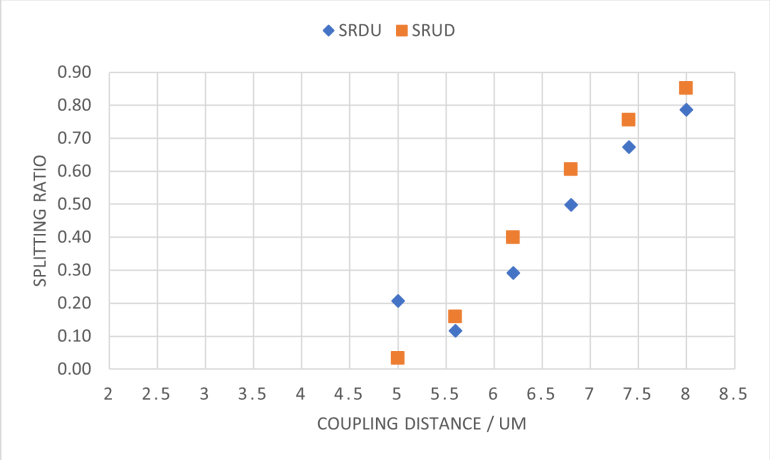

Figure 4.10: Comparison of the splitting ratio of directional couplers with opposite order of fabrication. DU stands for lower arm then upper arm and UD for the opposite.

The graph shows that the values of the coupling distances, to obtain the same splitting ratio, differ changing the order of the fabrication. This may result in a problem, it is difficult to get the correct coupling distance for both sets of couplers in a fabrication of a complete device, even if we fabricate multiple devices in one chip.

In the same fabrication of these couplers we tried also a different design for the 3D bent waveguides: the *Mantis* design. A plot of the final device with this layout is reported in Figure 4.11. With this layout the 3D waveguides bend just once, then go straight, above the other waveguides, and then bend down to return on the initial plane, with the rest of the guides, and form the last directional coupler. The lower number of curves of this waveguides may bring lower losses, considering that in the straight portion Borofloat has very low propagation losses. The drawback is that these guides has to travel a longer path in the vertical direction, to achieve the same distance to the waveguides that remain in plane. In the other design the bending of all the guides crossed reduced that. In the end this topology resulted in quite low losses, but the previous design ended up performing better.

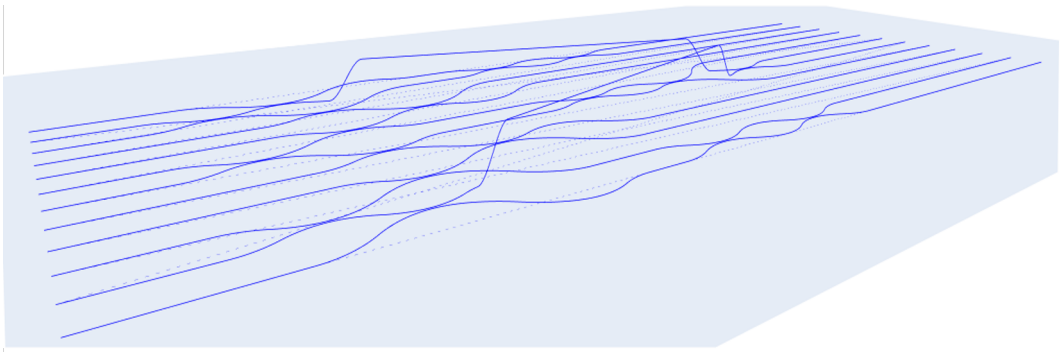

Figure 4.11: Mantis design of the final device. All the waveguides lies in the same plane, except for two of them, which bend up, then go straight and then return in plane to form the last coupler.

4.3.3. Final device characterization

The last fabrication of a set of complete devices we performed in Borofloat employed the initial layout, but with both 3D bent waveguides bending upwards. In neither of the device fabricated we were able to obtain a combination of low insertion loss and couplers with 50% splitting ratio. The best result we achieved is shown in the next plots.

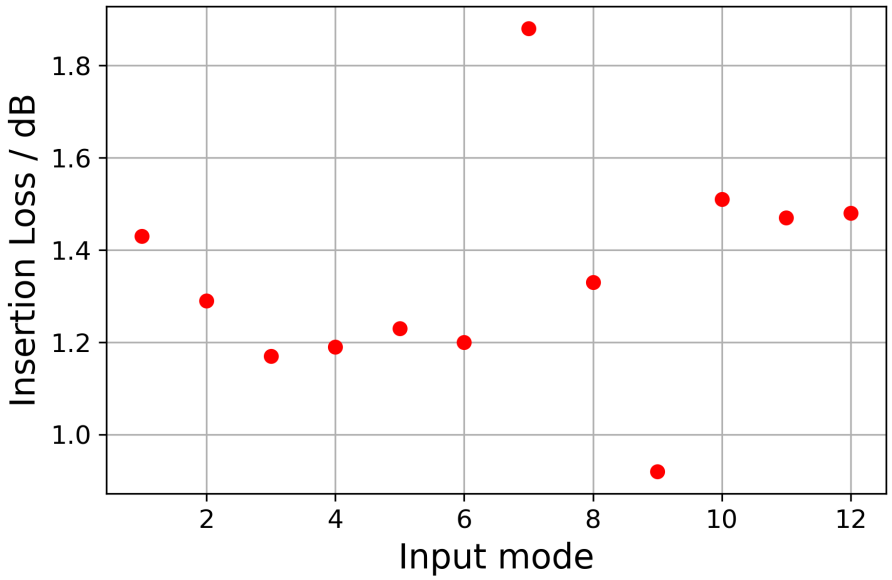

Figure 4.12: Insertion losses of the final device fabricated on Borofloat.

This time the insertion losses were much more in agreement with what we expected from the first waveguides optimization, but still a bit higher; in particular for the seventh mode the losses are much higher than the others. The directional couplers of this device have

splitting ratios around 55/45. This is not a very good result, but it is the best that we have obtained using Borofloat. A complete map of the power output of the device is shown in Figure 4.13.

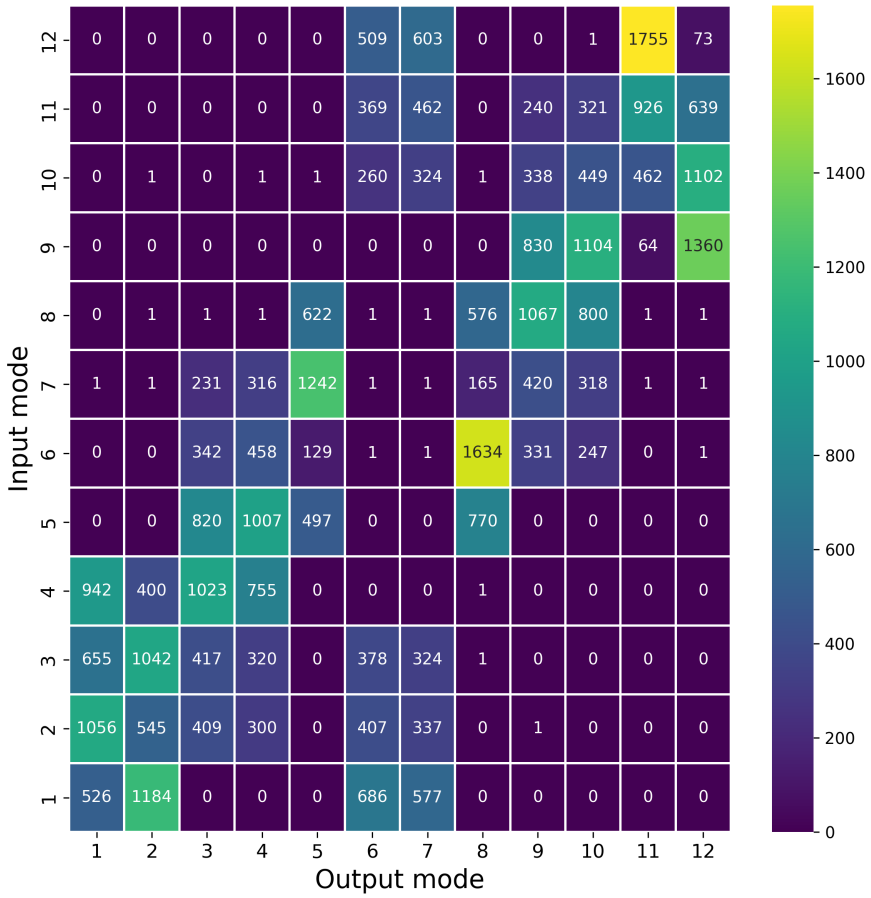

Figure 4.13: Power distribution of the final device obtained in Borofloat. It is colour coded for an easier visualization. A mirror symmetry with respect to the main diagonal should be visible with couplers' splitting ratio close to 50%.

4.3.4. Trenches fabrication

After the characterization of a complete device, if it is suitable, it has to be trenched. The trenches are structures made to thermally isolate a waveguide from the others. Such structures are needed when the thermal phase shifters are working. On Figure 4.1 are visible some black crosses, those are laser ablations. By focusing the laser beam, during the fabrication, on a face of the sample, it is possible to ablate the glass. These structures are visible with naked eye right after the procedure is completed. The trenches are done only on the suitable device on the chip, so after the characterization, in a successive fabrication with respect to the one where the device was fabricated. Those markers are

needed to align the sample, with the same reference of the previous fabrication.

In Borofloat the trenches have been demonstrated successfully. The repetition rate used is lower than the one to fabricate waveguides: 20KHz. The average powers measured at 1MHz rate were 1.1, 1.3 and 1.5 Watt. Images taken with the microscope are reported in figure 4.14.

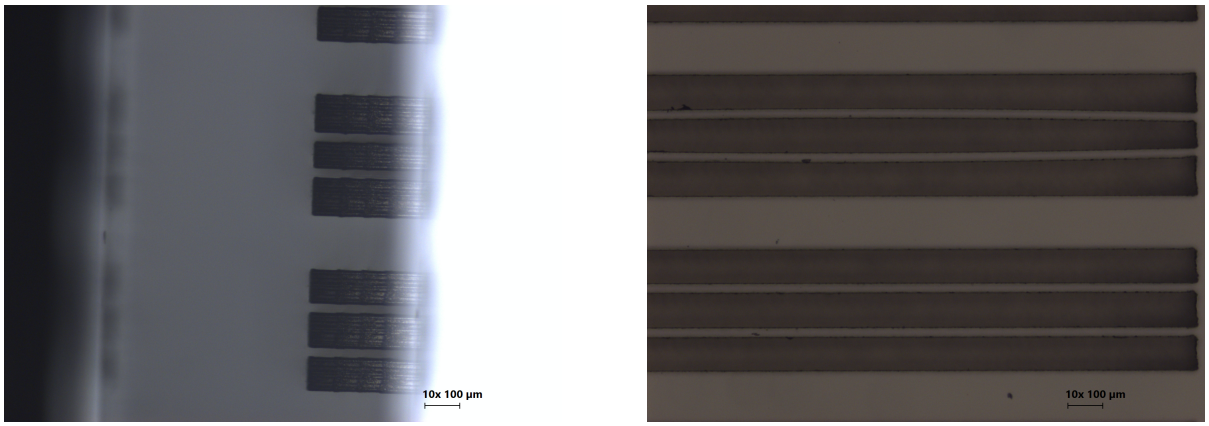

(a) Side view of the successful trenches on microscope.

(b) Top view of the successful trenches on microscope.

Figure 4.14: Successful trenches in Borofloat fabricated at 1.3W.

On those trenches have been performed an ultrasonic treatment after the fabrication. Five minutes in an acetone bath on an ultrasonic generator. This emptied the trenches from any undetached residual glass. From the image taken from the side of the trenches, the four *floors* which compose a trench are visible. For the first two the emptying yield is 100%, for the third floor is 75% and for the fourth is 50%. These data are gathered from a fabrication of 27 trenches on a Borofloat sample. After the ultrasonic bath, all the trenches are completely emptied. The drawback is that a collapse of the walls around the trenches may happen with this technique. An example is reported in figure 4.15. The trenches reported in this figure are the ones obtained with 1.5W. The others survived the ultrasonic treatment with no side effects, so we will use a power of 1.3mW to fabricate the trenches. Higher power gives an higher yield.

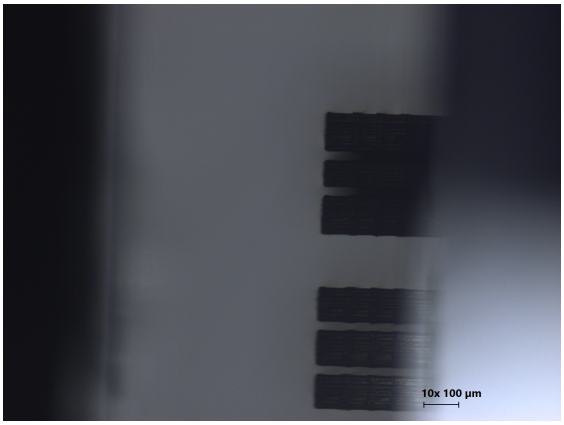

(a) Side view of the collapsed trenches on microscope.

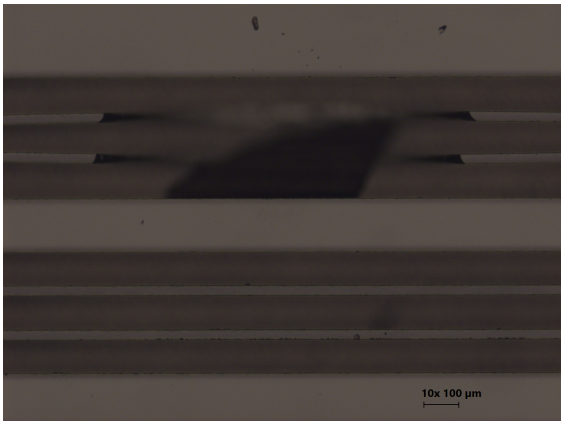

(b) top view of the collapsed trenches on microscope.

Figure 4.15: Collapsed trenches after the ultrasonic bath. In the upper group of trenches the walls are visibly collapsed in the center portion.

It has to be said that the ultrasonic treatment is not necessary for our device. This is because the procedure to deposit the thermal phase shifters is able to simultaneously empty the trenches.

4.3.5. Conclusions about Borofloat

In this section was presented all the work done with Borofloat. The steps between the different fabrications and the reasons behind all the choices made are still valid for the next section and the work done with EagleXG. We explored this glass and managed to demonstrate very low loss straight waveguides and bent waveguides with radii of at least 40mm.

The main problems with this substrate are two. First one is that it is very sensitive to the writing depth and the writing power. For a simpler device, with large bending only in plane and even an elongated structure, this glass can be very good and produce waveguides with very low losses compared to other substrates. The second issue, deeply connected with the first, is the reproducibility. We had hard times on trying to reproduce the guides we have found. This may be due to different factors, also the samples themselves and their relevant bending may have been the cause. In the future wider, depth stable, windows of fabrication have to be found, to make more complex devices and ensure the reproducibility of the recipes.

To conclude the work done with Borofloat did not produce the desired outcome, intended

as a final device with low losses and balanced couplers.

4.4. Fabrications in EagleXG glass

EagleXG is a glass that has been widely studied in the research group of Professor Osellame. It is already employed for the fabrication of a number of photonic integrated devices [9][8][31]. The key factor is that with EagleXG a more compact device can be fabricated. It has higher propagation losses with respect to Borofloat, but it has lower bending losses. In the next section the fabrication procedure to obtain the final device will be discussed, up to its characterization. The practical aspects were already discussed in the previous sections about the work with Borofloat, so I will focus more on the results achieved.

4.4.1. Waveguide optimization

The work with Borofloat continued until the laser Carbide remained available in the fabrication setup. When Pharos came back from repair, it was immediately reinstalled. With Pharos back we decided to give EagleXG a try. Being this glass widely employed by the reserach group, we didn't have to start from zero. Single mode waveguides, with low propagation losses, guiding at 925nm were already known. We kept the writing speed, number of scans and depth (the parameters of smaller impact on the insertion loss) from the already known recipe, and tried to optimize the power and the bending radius, focusing on the particular waveguides of our final device.

The writing depth in EagleXG can be calculated from the bottom facet of the sample, going upwards. This simplify a lot the fabrication procedure and it can be done in this way, with respect to Borofloat, because this glass is less sensitive to the writing depth and the recipes are more reproducible.

We performed a single optimization to find the parameters for the desired waveguide. We fabricated 3 sets of guides: straight waveguides (SWG), in plane bent waveguides (2DWG in Figure 4.2), and 3D bent waveguides (3DWG in Figure 4.2). These parameters were the cartesian product of

- 11 Powers (fromn 280mW to 380mW with jumps of 10mW)
- 3 Radii (20mm, 25mm, 40mm)

The results obtained are reported in Figure 4.16. The SWG losses are ranging from 0.81dB to 0.95dB, they are comparable to each other, showing the robustness of the recipe with respect to the tested parameters. To choose the best parameters to fabricate our final

device, we focused on the losses of the bent waveguides. The 3D bent one, as already discussed, is the waveguide with highest losses. In Figure 4.16c the losses of the 3D bent waveguides are reported. The one with the lowest losses is fabricated at 340mW and radius 25mm. The measured losses are 1.026dB.

Looking at the graph reporting the insertion losses of the waveguides bent in plane (Figure 4.16b), the same guide shows again the lowest losses between them all. Our choice was to keep these parameters and proceed towards the final device.

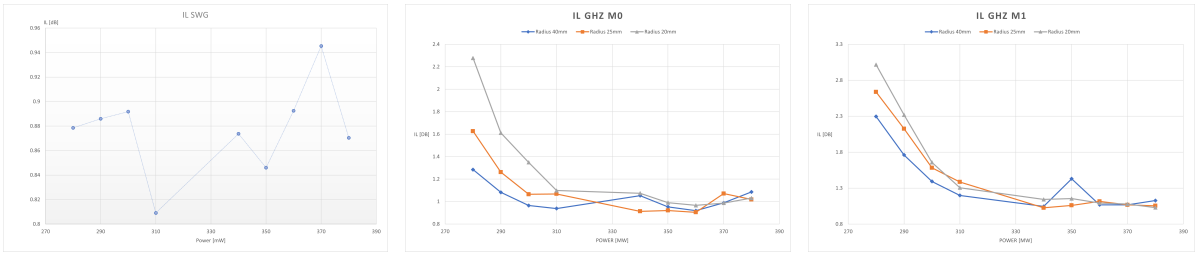

(a) Straight waveguides (b) In plane bent waveguides (c) 3D bent waveguides

Figure 4.16: Insertion losses of waveguides with different geometry. Data gathered for the optimization to find the parameter for the final waveguide. The highlighted points are the measured losses, the lines are just to guide the eyes.

4.4.2. Coupler optimization

The last step before the fabrication of the final device is the optimization of the couplers. They are made, as with Borofloat, with coupling length equal to zero, to minimize the dimension of the device. The parameter we control to adjust the splitting ratio is the coupling distance. We fabricated 13 couplers with coupling distances ranging from 0.003mm to 0.009mm. From the gathered data, about their splitting ratio as a function of the coupling distance, we were able to calculate the distance for the 50/50 coupler, by the already discussed fitting. The results regarding the couplers are reported in Figure 4.17. The calculated value of the coupling distance for the 50/50 coupler was d=*0.00572mm*.

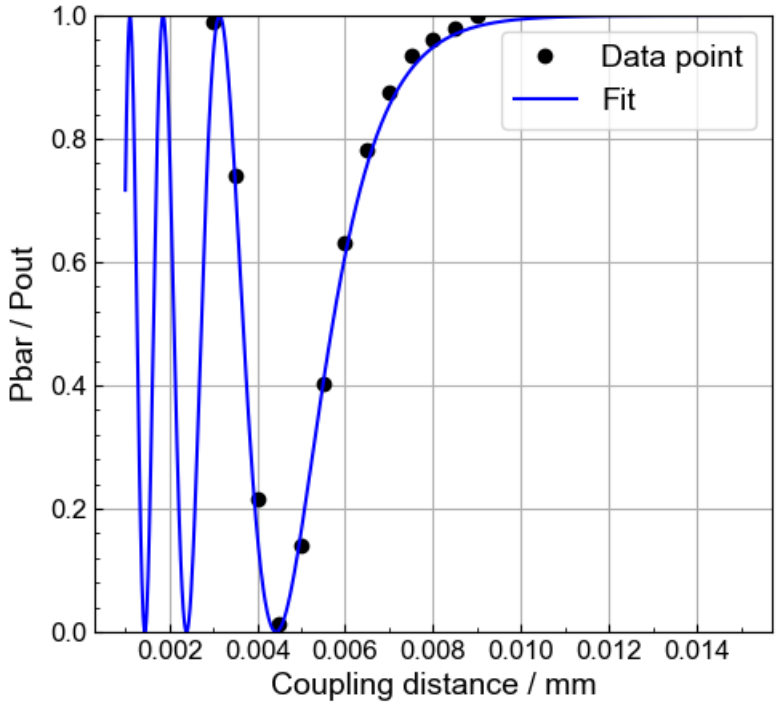

Figure 4.17: Function obtained from the fitting of the splitting ratio with respect to the coupling distance of the couplers fabricated in EagleXG.

4.4.3. Fabrication of the heralded GHZ state factory

Now that all the parameters had been found, we could proceed with the fabrication of the final device. Similarly to Borofloat five devices were fabricated on the same chip. The irradiation parameters are the same for all five. The difference lies in the coupling distances. From the data obtained by the fitting in Figure 4.17, we calculated the values corresponding to the 45/55 and 55/45 splitting ratios. The coupling distance of the directional couplers of each device is in this range, they are equally spaced by 60nm.

Device	1	2	3	4	5
Coupling distance (mm)	0.00560	0.00566	0.00572	0.00578	0.00584

Table 4.3: Coupling distances of the five devices fabricated in the final chip.

The fabrication layout is reported in Figure 4.18. There are the five devices, each spaced from the next by a straight waveguide, to simplify the characterization procedure and act as a reference. The laser starts before the beginning of the sample to ensure its arrival

on it with the open shutter. The sample was 5cm long. After the fabrication and the annealing procedure the sample was cut, on the right part, where the waveguides just go straight. It was then polished to be ready for the characterization and after these procedure its length is 3.3cm.

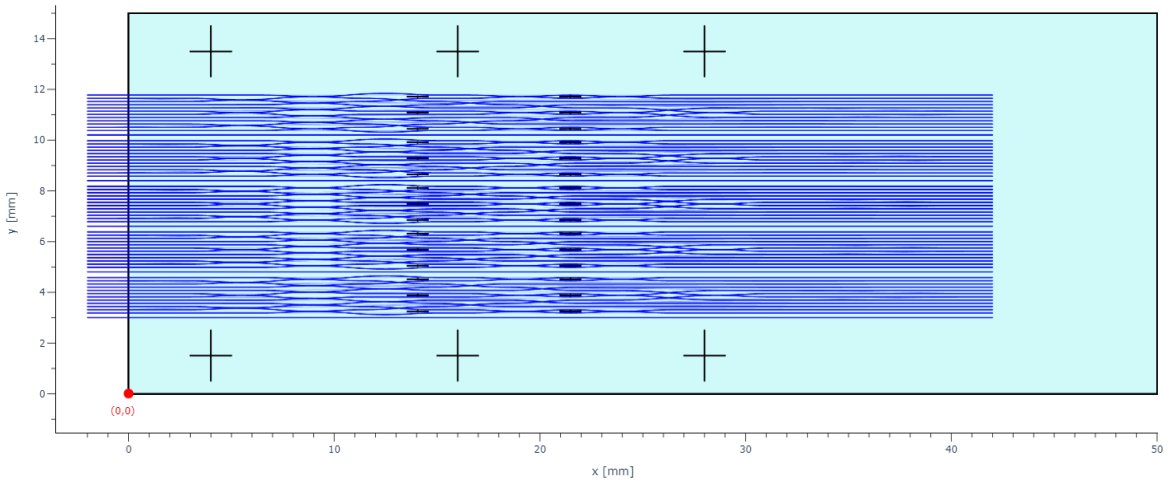

Figure 4.18: Complete fabrication of the final device.

The characterization involved all the devices, but we first checked the coupling ratios to find a suitable device, before measuring the losses. The obtained data and the discussion about the validation of the final device are reported in the next chapter.

The last procedure, involving the femtosecond laser micromachining technique, is the fabrication of trenches on the final device. The characterization confirmed that the fourth device, so the one with coupling distance d=0.00578mm, was the one with the couplers closer to 50% splitting ratio. So this was the one we trenched to prepare it to the deposition of the thermal phase shifters. A plot of the trenched device is reported in Figure 4.19.

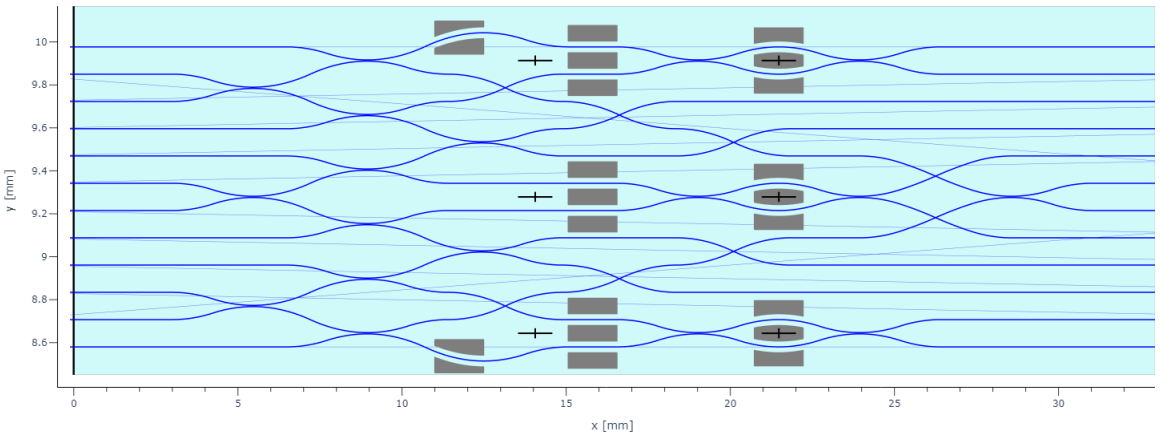

Figure 4.19: 2D layout of the final device including the trench structures (grey areas).

4.5. Conclusions

All the experimental procedures culminating in the fabricated final device were discussed in this chapter. First, the research for a suitable single mode waveguide at 925nm. Then optimizing the couplers to find a 50% splitting ratio and when all the parameters are chosen, the fabrication of the final device is performed. The work started with Borofloat glass. We explored this glass and fabricated a complete device with not optimal properties. Trying a different substrate, EagleXG, allowed for the fabrication of a suitable final device, which characterization is discussed in the next chapter. The design of the device underwent some changes in between different fabrication, but in the end the final device fabricated in EagleXG has the design reported and discussed in the first section of this chapter and also visible in Figure 4.19.

5 | Optical validation of the final device

In this chapter will be analyzed the complete device. In the first section its working principle is described form a theoretical point of view. Then the actual data gathered, to ensure its correct functioning, are shown and discussed. In the last section is presented the final device at the present stage of completeness.

5.1. Heralded GHZ factory, theoretical description

Up to this point I have presented all the experimental work done to fabricate the complete device, but never faced its functioning principles. I will now discuss all the components of the circuit, that starting from six identical photons produces the GHZ state and the heralders. These six identical photons are produced by high efficent single photon sources developed by another research group: Pascale Senellart group, from Center for Nanosciences and Nanotechnology CNRS at University Paris-Saclay. They have a technology based on quantum dots to produce single photons with high rates.

5.1.1. Circuit scheme

The scheme of the circuit is reported in Figure 5.1. On the left are labeled the twelve input modes, the black box represents the six single photon sources. The black lines are the waveguides and the black rectangles, where two guides crosses, are balanced beam splitters, that we implemented as 50/50 directional couplers. On the right half of the circuit the two couplers close together are Mach-Zehnder interferometers. They are used to perform a state tomography, after the generation of the GHZ state, so they are not involved in the generation of the state itself. On the far right there are the twelve output modes. They are labeled in pairs as Q_i, that stands for quibit i, and H_j that stands for heralder j. The heralders are the only one that will be measured, the black semi-circles represent the detectors. In the next paragraph the qubits and the heralding conditions

will be described in details. This scheme is the same one showed in the previous chapters, a coupler has just been moved in line with the others, without changing anything in the circuit, to better visualize the overall composition and the different stages. The circuit is symmetric, the first six modes are equal to the last six mirrored.

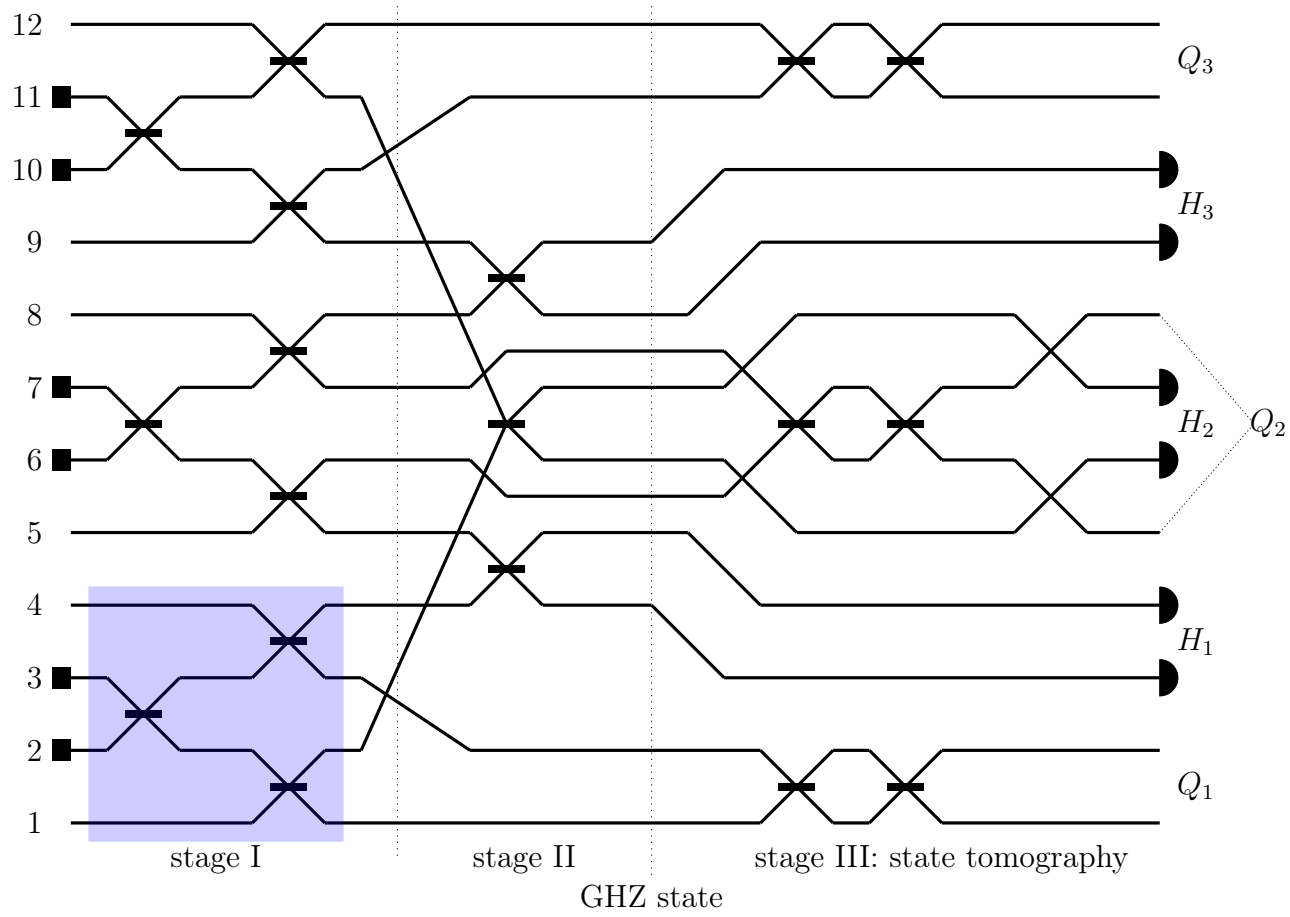

Figure 5.1: Scheme of the circuit. The black lines are the waveguides, the black rectangles where the guides cross are balanced beam splitters. The black squares on the left are the single photons inputs of the circuit, the semi-circles on the right are the detectors. Three different stages are highlighted. The labels H_j stands for heralder j, while Q_i stands for qubit i.

Qubits definition:

For our device we decided to define the qubits with a spatial encoding, so the presence of a photon in a certain mode and not in another. The definitions are the following:

$$|0\rangle_1 = |0_1 1_3\rangle \qquad |1\rangle_1 = |1_1 0_3\rangle$$
$$|0\rangle_2 = |0_6 1_7\rangle \qquad |1\rangle_2 = |1_6 0_7\rangle$$
$$|0\rangle_3 = |0_{10} 1_{12}\rangle \qquad |1\rangle_3 = |1_{10} 0_{12}\rangle$$

the label of the ket is the number of the qubit defined in Figure 5.1, the numbers inside the ket represent the presence (1) or absence (0) of a photon in the channel indicated by its respective label, referred to the input modes. The definition of a GHZ state given with the qubits is:

$$|GHZ_{\pm}\rangle = \frac{1}{\sqrt{2}}\Big(|000\rangle \pm |111\rangle\Big) \tag{5.1}$$

so this means having a superposition of states with the three qubits all equal to 0 and all equal to 1.

Heralders definition:

To ensure the production of the correct state we have some heralders. These are measured by six detectors and the condition they must satisfy to herald the presence of a GHZ state is to have one and only one detector clicking for each pair of every heralder. There are then eight possible combinations that satisfy this condition and are the following:

$$|h_1\rangle = |0_4 1_5 0_2 1_{11} 0_8 1_9\rangle \qquad |h_2\rangle = |0_4 1_5 0_2 1_{11} 1_8 0_9\rangle$$
$$|h_3\rangle = |0_4 1_5 1_2 0_{11} 0_8 1_9\rangle \qquad |h_4\rangle = |0_4 1_5 1_2 0_{11} 1_8 0_9\rangle$$
$$|h_5\rangle = |1_4 0_5 0_2 1_{11} 0_8 1_9\rangle \qquad |h_6\rangle = |1_4 0_5 0_2 1_{11} 1_8 0_9\rangle$$
$$|h_7\rangle = |1_4 0_5 1_2 0_{11} 0_8 1_9\rangle \qquad |h_8\rangle = |1_4 0_5 1_2 0_{11} 1_8 0_9\rangle$$

the numbers in the ket indicate the presence or absence of a photon in the respective labeled mode. The following calculations will demonstrate that the heralding conditions just reported ensure the presence of a GHZ state in the remaining modes.

5.1.2. Stage I calculations

The circuit can be decomposed in three identical parts, each formed by four input modes. In stage I, for each group of four input modes, we have the same topology formed by three directional couplers. In the subsequent stages it is harder to visualize this symmetry, because some of the guides are deviated with respect to others to fit the device in the smallest possible chip. Considering that all the couplers are ideally balanced beam

splitters, the circuit has in fact some modularity: the series of transformations to which the modes 1-4 undergo, is the same of the modes 5-8 and again 9-12. For this reason I will go through the calculations for only one group of four modes, the result for the other will be completely similar.

The input of the complete device is

$$|Device - input\rangle = |0_1 1_2 1_3 0_4 0_5 1_6 1_7 0_8 0_9 1_{10} 1_{11} 0_{12}\rangle \tag{5.2}$$

so for the highlighted group in Figure 5.1 with a blue square , and respectively each other group, the input corresponds to

$$|Group - input\rangle = |0110\rangle = \hat{a}^\dagger_{2,in}\hat{a}^\dagger_{3,in}\,|0000\rangle \tag{5.3}$$

in the last term the creation operators have been used. In this first stage the state passes through three 50/50 directional couplers between different modes. This can be represented as a 4x4 unitary matrix, acting on the creation operators.

$$U = \frac{1}{\sqrt{2}}\begin{pmatrix} 1 & i & 0 & 0 \\ i & 1 & 0 & 0 \\ 0 & 0 & 1 & i \\ 0 & 0 & i & 1 \end{pmatrix} \cdot \begin{pmatrix} 1 & 0 & 0 & 0 \\ 0 & \frac{1}{\sqrt{2}} & \frac{i}{\sqrt{2}} & 0 \\ 0 & \frac{i}{\sqrt{2}} & \frac{1}{\sqrt{2}} & 0 \\ 0 & 0 & 0 & 1 \end{pmatrix} = \frac{1}{2}\begin{pmatrix} \sqrt{2} & i & -1 & 0 \\ i\sqrt{2} & 1 & i & 0 \\ 0 & i & 1 & i\sqrt{2} \\ 0 & -1 & i & \sqrt{2} \end{pmatrix} \tag{5.4}$$

This matrix transforms the input state creation operators into the output state ones. What is obtained then is:

$$\hat{a}^\dagger_{2,in} \to \frac{1}{2}\cdot\left(i\hat{a}^\dagger_{1,out} + \hat{a}^\dagger_{2,out} + i\hat{a}^\dagger_{3,out} - \hat{a}^\dagger_{4,out}\right)$$
$$\hat{a}^\dagger_{3,in} \to \frac{1}{2}\cdot\left(-\hat{a}^\dagger_{1,out} + i\hat{a}^\dagger_{2,out} + \hat{a}^\dagger_{3,out} + i\hat{a}^\dagger_{4,out}\right)$$

Substituting this in 5.3, performing all the products and rearranging the terms the following result is obtained

$$|Group - output\rangle = -\frac{1}{2}\Big(|1100\rangle + |0011\rangle\Big) + \frac{i\sqrt{2}}{4}\Big(-|2000\rangle + |0200\rangle + |0020\rangle - |0002\rangle\Big) \tag{5.5}$$

At this point we have to consider the output states also of the other groups, because they mix together in the next stage. This leads to a long and complicated expression, but it can be simplified. We neglect all the terms that will produce a wrong combination of outputs, not respecting the heralding conditions. Can be demonstrated that all the states with two photons in the same channel produce a non correct heralding output, regardless the output state of the other groups, thus we can discard all these terms. We are left with only the terms in the first parenthesis of Eq. 5.5. We have to combine these terms for the three groups to get the complete state after stage I. It is given by their tensor product:

$$\frac{1}{2}\Big(|1100\rangle + |0011\rangle\Big)_{groupA} \otimes \frac{1}{2}\Big(|1100\rangle + |0011\rangle\Big)_{groupB} \otimes \frac{1}{2}\Big(|1100\rangle + |0011\rangle\Big)_{groupC} \tag{5.6}$$

Again some terms that leads to two photons in the heralding channels can be discarded and we are left with the only two states that respect the heralding conditions:

$$|StageI - output\rangle = \frac{1}{8}\Big(|1_1 1_2 0_3 0_4 1_5 1_6 0_7 0_8 1_9 1_{10} 0_{11} 0_{12}\rangle + |0_1 0_2 1_3 1_4 0_5 0_6 1_7 1_8 0_9 0_{10} 1_{11} 1_{12}\rangle\Big) \tag{5.7}$$

5.1.3. Stage II calculations and final output

Eq. 5.7 are the two states, after stage I, that can produce the correct heralding condition at the output of the device. The last transformation they undergo is given by stage II (as already said the last stage is just for state tomography and does not influence the final output). In this part of the circuit three more 50/50 directional couplers are present. They act as balanced beam splitters, so their output is given by the following relations:

$$BS_{i,j}\,|0_i 1_j\rangle \rightarrow \frac{1}{\sqrt{2}}\Big(|0_i 1_j\rangle + |1_i 0_j\rangle\Big)$$
$$BS_{i,j}\,|1_i 1_j\rangle \rightarrow \frac{i}{\sqrt{2}}\Big(|0_i 2_j\rangle + |2_i 0_j\rangle\Big)$$

So we have to apply these to the correct modes of the output state of stage I. As can be seen in Figure 5.1, in stage II we have $BS_{2,11}$, $BS_{4,5}$ and $BS_{8,9}$. The result is the following:

$$|StageII-output\rangle = \frac{1}{16\sqrt{2}}\Bigg(|1_1 0_3\rangle \Big[|0_4 1_5\rangle + i\,|1_4 0_5\rangle\Big] \otimes |1_6 0_7\rangle \Big[|0_8 1_9\rangle + i\,|1_8 0_9\rangle\Big] \otimes \\ \otimes |1_{10} 0_{12}\rangle \Big[|0_2 1_{[}11]\rangle + i\,|1_2 0_{11}\rangle\Big] + \\ + |0_1 1_3\rangle \Big[|1_4 0_5\rangle + i\,|0_4 1_5\rangle\Big] \otimes |0_6 1_7\rangle \Big[|1_8 0_9\rangle + i\,|0_8 1_9\rangle\Big] \otimes \\ \otimes |0_{10} 1_{12}\rangle \Big[|1_2 0_{11}\rangle + i\,|0_2 1_{11}\rangle\Big]\Bigg)$$

The modes in the ket multiplying the square brackets represent the quibits, as defined at the beginning of this section. We can rearrange the terms to better visualize the output states:

$$|StageII-output\rangle = \frac{1}{16\sqrt{2}}\Bigg(|111\rangle_{qb} \Big[|0_4 1_5\rangle + i\,|1_4 0_5\rangle\Big]\Big[|0_8 1_9\rangle + i\,|1_8 0_9\rangle\Big]\Big[|0_2 1_{11}\rangle + i\,|1_2 0_{11}\rangle\Big] + \\ + |000\rangle_{qb} \Big[|1_4 0_5\rangle + i\,|0_4 1_5\rangle\Big]\Big[|1_8 0_9\rangle + i\,|0_8 1_9\rangle\Big]\Big[|1_2 0_{11}\rangle + i\,|0_2 1_{11}\rangle\Big]\Bigg)$$

The states $|111\rangle_{qb}$ and $|000\rangle_{qb}$ are the logical states of the qubits obtained, the remaining terms in the square brackets are the heralder states. By using the definition of the heralding conditions given above we can rewrite these states to get the final result comprehending all the outputs:

$$|StageII-output\rangle = \frac{1}{16\sqrt{2}}\Bigg(\Big[|111\rangle_{qb} - i\,|000\rangle_{qb}\Big]\,|h_1\rangle + \Big[i\,|111\rangle_{qb} - |000\rangle_{qb}\Big]\,|h_2\rangle + \\ + \Big[i\,|111\rangle_{qb} - |000\rangle_{qb}\Big]\,|h_3\rangle + \Big[-|111\rangle_{qb} + i\,|000\rangle_{qb}\Big]\,|h_4\rangle + \\ + \Big[i\,|111\rangle_{qb} - |000\rangle_{qb}\Big]\,|h_5\rangle + \Big[-|111\rangle_{qb} + i\,|000\rangle_{qb}\Big]\,|h_6\rangle + \\ + \Big[-|111\rangle_{qb} + i\,|000\rangle_{qb}\Big]\,|h_7\rangle + \Big[-i\,|111\rangle_{qb} + |000\rangle_{qb}\Big]\,|h_8\rangle\Bigg)$$

These are the output states qubits obtained with their respective heralding condition. These are all GHZ states, is sufficient to apply a phase shift on the correct channels to retrieve the expression of Eq. 5.1. Applying a $\frac{\pi}{2}$ phase shift is equivalent to multiply the state by i. This can be easily done in the circuit exploiting the thermal phase shifters

placed on the Mach-Zehnder interferometers of stage III. With this trick the final result is the following:

$$|Final-output\rangle = \frac{1}{16}\Big(-|GHZ_-\rangle\,|h_8\rangle + |GHZ_-\rangle\,\Big[|h_2\rangle + |h_3\rangle + |h_5\rangle\Big] + \\ -i\,|GHZ_+\rangle\,|h_1\rangle + i\,|GHZ_+\rangle\,\Big[|h_4\rangle + |h_6\rangle + |h_7\rangle\Big]\Big)$$

so based on the heralding condition we get a GHZ state with a certain global phase, that does not influence the state itself. It is also possible to switch between $|GHZ_-\rangle$ and $|GHZ_+\rangle$ by applying a π phase shift to the correct channels, which correspond to a multiplication by -1 of one of the state of three qubits. All the phase shifting can be dynamically employed by the fast thermal phase shifters after the measurement of the heralders.

5.1.4. Real case discussion

At this point we have demonstrated the feasibility of the circuit in the production of GHZ states, considering all the elements ideal. The success rate of this circuit in generating a GHZ state is $p = \frac{8}{16^2} = \frac{1}{32}$. This is due to the post selection done after stage I. An high injection rate of single photons can lead to a consistent rate of production of GHZ states, this is why we rely on the single photon sources studied by the above mentioned french research group, which can achieve high generation rate.

A remark has to be done regarding the phase accumulated by the different modes. This may be given by some variability in the fabrication process. We are not interested in the precise phase of each mode, it is not accessible and in general the global phase of the output does not modify it. What may influence the output of our circuit is the phase difference between different modes. Can be demonstrated that in the end, all the phase differences between every mode give a contribution that can be grouped to achieve a state of the type:

$$|GHZ_\pm(\theta)\rangle = \frac{1}{\sqrt{2}}\Big(|111\rangle \pm e^{i\theta}\,|000\rangle\Big) \tag{5.8}$$

this can be compensated using the thermal phase shifters, in this way it is possible to retrieve an output state as defined in 5.1. The heralding conditions are not affected by the phase shifts, so the circuit is able to work as described in the previous paragraphs.

Having the heralders that confirm the presence of the correct state, we are not afraid of

photon losses too. A loss of a photon can lead only to two possibilities: an heralders detection that do not satisfy the heralding conditions, so we can just discard this states, even if it can be actually a GHZ state; or an heralders detection that satisfy one of the conditions, but the output state of the qubits has less than three photons, so we just have to discard all the states that do not conserve the initial photon number. In conclusion the losses in our device reduce the generation rate of GHZ states, but when we detect the correct conditions, we are sure that the generated state is the correct one.

5.2. Final device characterization

Now that we have discussed the theory behind the device and demonstrated that it is capable to realize our goal, we can proceed to its actual characterization. In this section the results of the optical characterization of the final device are presented. The insertion losses, the splitting ratio of the couplers and also some polarization measurements.

5.2.1. Directional couplers

The first measurement done on the final device, after a visual check with the microscope and the polishing procedure to minimize the coupling losses, was the splitting ratio of the couplers. We did this by reversing the device, so we coupled the optical fiber with the output facet and collected the radiation from the input facet. In this way it has been possible to gather information about more directional couplers. For example, right before the input facet, which is our output in this configuration, there are the couplers of stage I. Some of these couplers split the incoming power and then it is immediately collected by the objective and focused on the powermeter. By measuring these powers, the splitting ratio of the respective couplers is easily accessible. It is also possible to measure the splitting ratio of the same coupler entering from different channels and so being able to confront them and check if some differential losses are present.

With the backward characterization we decided which device to trench and after this second fabrication procedure, we performed a characterization of the device entering from the actual input facet. This allowed us to access all the couplers we wanted. We ignored the ones forming the Mach-Zenhder interferometers, because we cannot access them individually and they are needed for the state tomography, not the actual state generation. The results of the splitting ratio of the couplers is reported in Figure 5.2, with reference to Figure 5.3. We performed the average of the splitting ratio measured that we have accessed from multiple channels, to have more consistent results.

Coupler	Splitting ratio
1	50.39%
2	50.95%
3	49.46%
4	50.68%
5	51.20%
6	50.84%
7	48.76%
8	50.70%
9	48.91%
10	50.74%
11	46.49%
12	48.89%

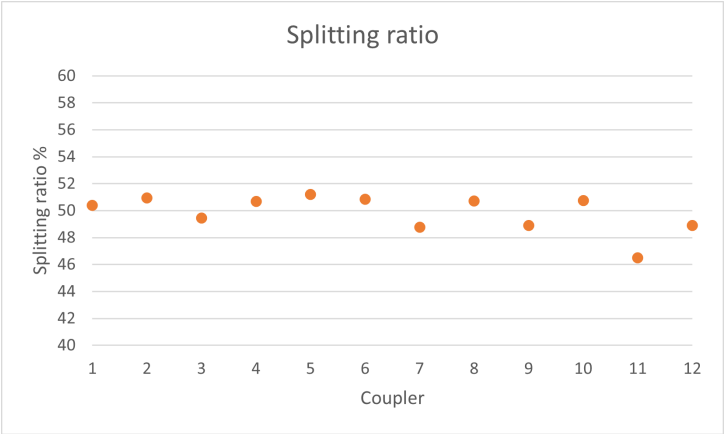

Figure 5.2: Splitting ratio with reference to Figure 5.3.

For all the couplers the spltting ratio measured did not highlight the presence of differential losses. All the measures gave results on the splitting ratio very close to 50%. The values ranged from 48.76% to 51.20%, except for one particular coupler, for which we measured a splitting ratio of 46.49%. This coupler is the last one fabricated, between the modes 2 and 11. A possible explanation for this difference with respect to all the other couplers, may be found in the fabrication procedure. Due to the fixed order of fabrication we must follow, all the modes are fabricated in sequence, so all the coupers are fabricated with a small time interval between the lower arm and the upper arm. This is given just by the time of positioning the stage, from the ending of one guide to the beginning on the next one. This is not valid only for the different coupler, for which the upper arm is fabricated after a time corresponding to the fabrication time of 8 other modes. This is around 5 minutes, to be compared with just seconds for the other couplers. It is possible that a drift of the stage slightly modified the coupling distance and this resulted in a different splitting ratio.

Measurements with a controlled polarization of incident light, in two orthogonal directions, were also performed. The splitting ratio showed no dependence on the direction of the polarization and the values remained equal to the ones measured with light polarized at a random direction.

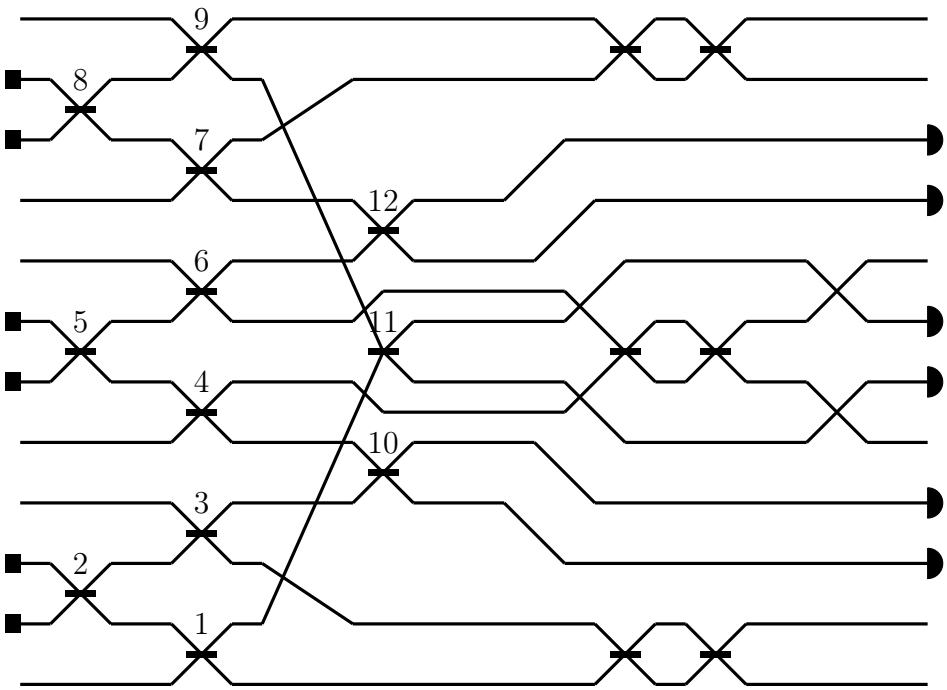

Figure 5.3: Schematics of the circuit to highlight the directional couplers.

5.2.2. Insertion Losses

With the setup described in chapter 3 the insertion losses of the final device were measured. For each input, the power at each output has been measured, always correcting the resulted losses with the reference power measured at the 10% output of the 90/10 coupler, placed before the optical fiber. The measurement of both losses and couplers splitting ratio where done also while controlling the polarization of the incident light. This has been done to ensure that there is no dependence on the particular polarization of the radiation with the outcome of the circuit. This dependence may be due to a birefringence of the waveguides, which is possible to obtain with femtosecond laser micromachining, so we performed this control on our device.

These results are reported in Figure 5.4 and 5.5. There are slightly changes in the losses measured with the two polarization, but are within the experimental uncertainty. For all the modes the losses are lower than 1.25dB. Again the worst mistake we are making is overestimating the losses, so in the worst scenario the chip is better than what we measured. The power distribution over all the modes (coloured charts) are symmetrical, with respect to their principal diagonal, as they should be. The circuit is symmetrical and so must be its output, if the beam splitters are balanced and the waveguides have comparable losses. The only part that is not symmetrical is the output of the Mach-

Zehnder interferometers, but this is expected and they can be tuned later with the thermal phase shifters.

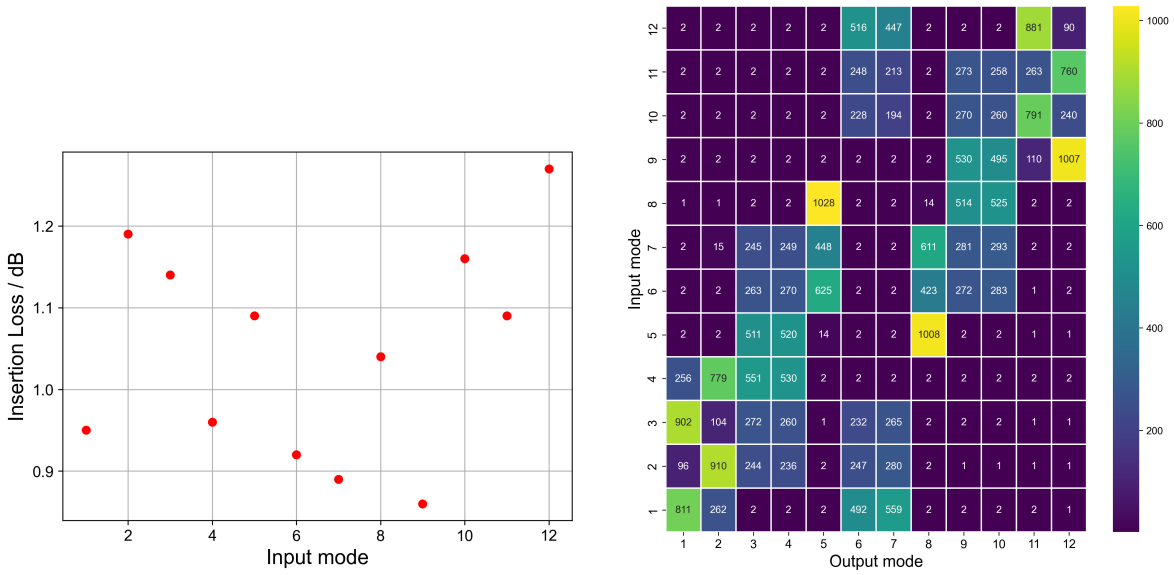

(a) (b)

Figure 5.4: Power distribution and insertion losses of the final device measured with vertical polarization.

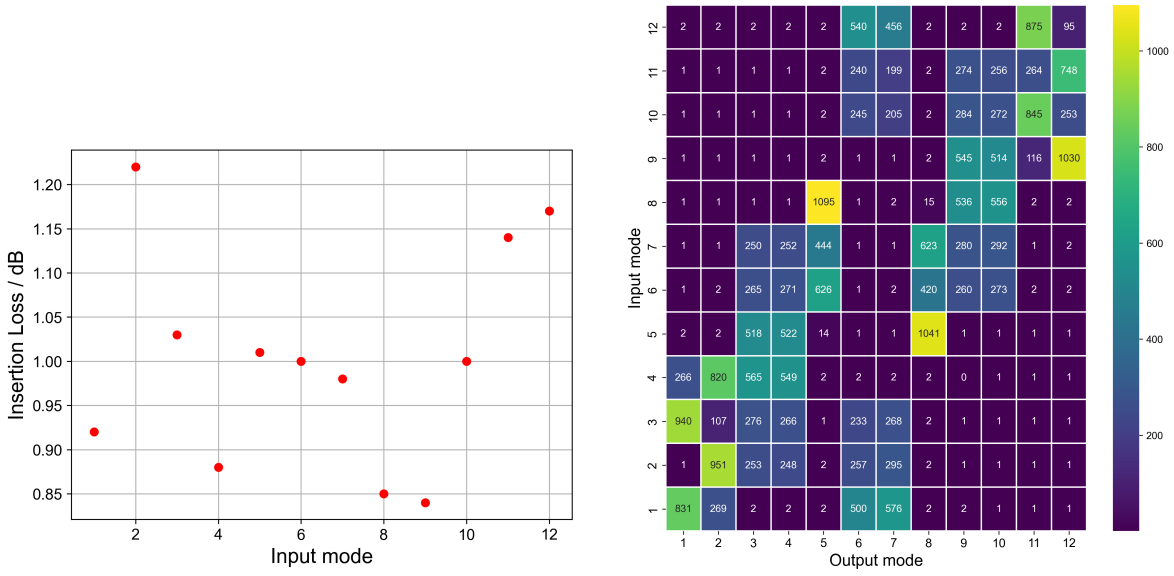

(a) (b)

Figure 5.5: Power distribution and insertion losses final device measured with horizontal polarization.

The effect of photon losses is to reduce the generation rate of GHZ states. Considering perfect single photon sources and detectors, our circuit has the following probability to produce the wanted state. As already discussed the probability of measuring a correct heralding condition is $p_h = \frac{1}{32}$=0.03125. The probability of maintaining six photons from the input to the output of the device can be estimated considering the average losses of each mode of the device ≈1dB. This gives a probability $p_l = (10^{-0.1})^6$. Multiplying these two factors we obtain the rate of success of our device as $p_s = p_h p_l \simeq 0.0785$. This is not so low as it seems. Of course we have to consider also the success rate of the sources and detectors of single photons [38], this gives an overall success rate $\simeq 10^{-3}$. This result is something usable in principle for quantum computing. Different protocols have been developed to achieve quantum computation below a certain threshold of photon losses [33], [5]. The advantage of using a cluster state, to implement a quantum computer, is that we can employ any methods to build it and only after that the computation starts, so photon losses at this stage are not something restrictive for the success of the computation. The insertion losses achieved with this device are a step forward with respect to other chips produced before. In the future a further reduction of the losses may be possible, leading to an higher rate of generation of GHZ states.

5.3. Thermal phase shifters and complete device

When the characterization of the device is complete and it is confirmed to be a suitable candidate for a final chip, it undergoes the procedures to implement the thermal phase shifters. This process has been realized in Polifab by means of lithography in a clean room. A total of 14 resistors have been deposited on top of the chip, precisely above the waveguides and in between the trenches. These resistances have been tested and all work properly.

An issue encountered after the resistances development is a systematic increase of the insertion losses of the device of ≈ 1dB. This is due to a layer of Si_3N_4 covering the input and output facets of the chip. The thickness of this layer provides an high reflectivity to a wavelength of 925nm, which is exactly the one we use. This layer was not deposited on purpose on these facets, but the procedures to grow the resistances are made to work on big wafers, which will be cut into small chips later on, so there is no reason to worry about the borders of the wafer, they will be thrown away after the cutting. For our chip is different, it enters the clean room already in its final shape.

A solution to overcome this problem is to remove this layer with a procedure similar to the polishing one, just a sand paper disk eroding this coat. It may be difficult to understand

when the layer is completely removed or if we are damaging the glass, so a less risky solution is the index matching. A liquid substance is applied to the face of the chip and when it is solidified its refractive index match very closely the one of the glass. For a different chip of the research group this procedure brought the transmission of the chip back to its value before the lithographic treatment. We are confident that this result can be replicated on our chip.

As can be seen in Figure 5.6 the chip is mounted on two holders made of Aluminum screwed together. They are needed to be able to anchor the chip to the optical table and, more importantly, to hold in position a Peltier cell [43] below the chip. This is used to control the temperature of the whole chip and keep it stable.

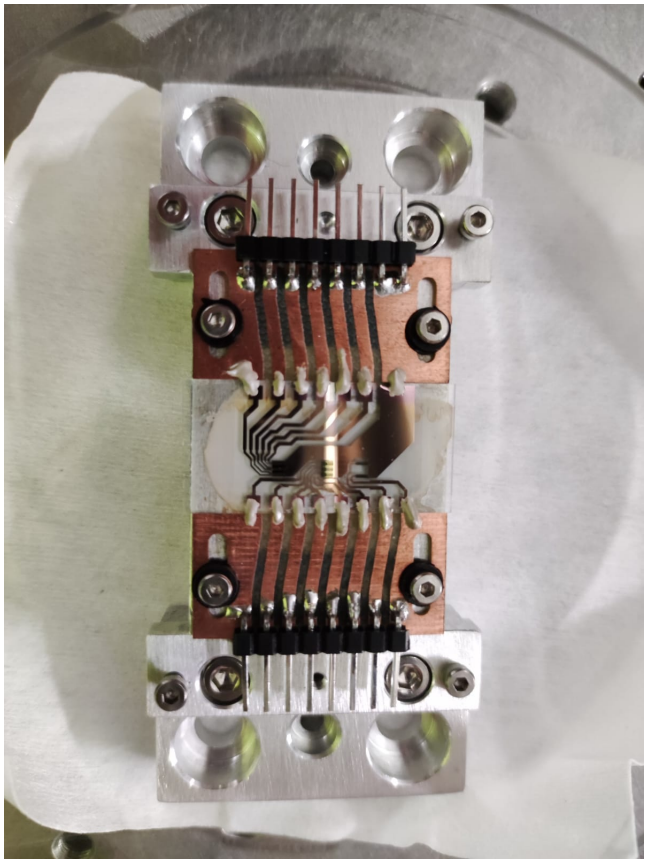

Figure 5.6: Picture of the final device. In the middle is present the device itself with the metallic contacts on top. It is mounted on a metallic support that can be anchored to an optical table or the characterization set-up.

At the moment of the writing of this thesis the chip is at this stage. Once the issue caused by the Si_3N_4 layer will be solved, the chip will undergo a procedure called pigtailing. Two fiber array (each composed by 12 optical fiber attached together) will be glued to the 12

modes at the input and the output of the device. To do this is used a particular glue, which is a viscous liquid, but solidify after the exposure to UV light. The refractive index of the solidified glue is close to the one of the glass to maximize the transmission.

The last procedure that will be performed on the device is a characterization of the thermal phase shifters. This is needed to find the currents that need to be injected in the resistances to achieve the phase shift desired.

5.4. Conclusions

The final device functioning principle has been discussed and the optical characterization confirmed that the device fabricated works as expected. It is suitable to produce the desired state at a rate $\approx 10^{-3}$ with the sources and detectors developed by Pascale Senellar research group. This is possible because the insertion losses are lower than 1.25dB for each mode and the couplers splitting ratio is close to 50% for all but one. The metallic resistances and contacts have been fabricated and the device is almost ready to use. The final procedure of pigtailing and then a characterization of the thermal phase shifter will be carried out in the following weeks after the publication of this thesis.

6 | Conclusions and future work

In this thesis has been presented the work done to achieve an integrated photonic circuit for the generation of heralded GHZ states. Having a fast and consistent way of generating this particular state is of great importance for the development of a photonic measurement based quantum computer. This state is the basic building block for the cluster state, from which all the computation begins. The device was fabricated employing the femtosecond laser micromachining technique, which consists in focusing ultrashort laser pulses on a glass substrate to induce refractive index changing.

The initial optimization process with Borofloat glass led to unsatisfying results. Nonetheless we have explored this glass and some data obtained highlight the possibility to fabricate interesting devices with it in the future. The second part of the work was done with EagleXG glass, this led to much more satisfying results. We obtained a final device, with the properties highlighted in the last chapter. All the modes have insertion losses lower than 1.25dB, a result compatible with our initial goal. The optical characterization proved that the device works as expected. A final procedure regarding the tuning of the phase shifters is yet to be performed, but the resistances have been checked to work properly. After this the device is ready to be tested with single photon sources, to actually fulfill its purpose in generating GHZ states. These can be useful not only for quantum computing, but also for other experiments or protocols involving entangled states.

The field of integrated photonic circuits is developing fast. Many different devices have already been fabricated and research to improve those and to make others is constantly performed. In the future a device to generate heralded GHZ states, with lower losses than the one we achieved, could be fabricated; maybe exploiting Borofloat glass as a substrate, after a good and reliable recipe is found. This would improve the generation rate of the states. The search for always better performing device would lead also to better components of a whole photonic quantum computer and in general better photonic devices useful in many different fields.

Bibliography

[1] A. Arriola, S. Gross, N. Jovanovic, N. Charles, P. G. Tuthill, S. M. Olaizola, A. Fuerbach, and M. J. Withford. Low bend loss waveguides enable compact, efficient 3d photonic chips. *OPTICS EXPRESS*, 21, 2013.

[2] G. Benenti, G. Casati, and G. Strini. *Principle of Quantum Computation and Information, Volume I and II.* World Scientific Publishing Co. Singapore 596224, 2007.

[3] C. H. Bennett, S. Popescu, D. Rohrlich, J. A. Smolin, and A. V. Thapliyal. Exact and asymptotic measures of multipartite pure-state entanglement. *Physical Review A*, 63, 2000.

[4] N. Bergamasco, M. Menotti, J. E. Sipe, and M. Liscidini. Generation of path-encoded greenberger-horne-zeilinger states. *Physical Review Applied*, 8, 2017.

[5] H. J. Briegel, D. E. Browne, W. Dür, R. Raussendorf, and M. V. den Nest. Measurement-based quantum computation. *Nature physiscs*, 5, 2009.

[6] D. E. Browne and T. Rudolph. Resource-efficient linear optical quantum computation. *Physical Review Letter*, 95, 2005.

[7] F. Ceccarelli, S. Atzeni, A. Prencipe, R. Farinaro, and R. Osellame. Thermal phase shifters for femtosecond laser written photonic integrated circuits. *Journal of Lightwave Technology*, 37, 2019.

[8] F. Ceccarelli, S. Atzeni, C. Pentangelo, F. Pellegatta, A. Crespi, and R. Osellame. Low power reconfigurability and reduced crosstalk in integrated photonic circuits fabricated by femtosecond laser micromachining. *Laser Photonics Review*, 14, 2020.

[9] A. Crespi, R. Osellame, and F. Bragheri. Femtosecond-laser-written optofluidics in alumino-borosilicate glass. *Optical Materials: X*, 4, 2019.

[10] S. M. Eaton, H. Zhang, P. R. Herman, F. Yoshino, L. Shah, J. Bovatsek, and A. Y. Arai. Heat accumulation effects in femtosecond laserwritten waveguides with variable repetition rate. *OPTICS EXPRESS*, 13, 2005.

[11] A. Einstein, B. Podolsky, and N. Rosen. Can quantum-mechanical description of physical reality be considered complete? *Physical Review*, 47, 1935.

[12] M. Fox. *Quantum Optics: an Introduction*. Oxford University Press, 2006.

[13] R. R. Gattass and E. Mazur. Femtosecond laser micromachining in transparent materials. *Nature photonics*, 2, 2008.

[14] N. Gisin and H. Bechmann-Pasquinucci. Bell inequality, bell states and maximally entangled states for n qubits. *Physics Letters A*, 246, 1998.

[15] F. Giustino and et al. The 2021 quantum materials roadmap. *JPhys Materials*, 3, 2021.

[16] D. M. Greenberger, M. A. Home, and A. Zeilinger. Bell's theorem quantum theory and conceptions of the universe, going beyond bell's theorem. *Springer*, 37, 1989.

[17] H. E. Hagy. Fine annealing of optical glass for low residual stress and refractive index homogeneity. *Applied Optics*, 7, 1968.

[18] H. Hu¨bel, D. R. Hamel, A. Fedrizzi, S. Ramelow, K. J. Resch, and T. Jennewein. Direct generation of photon triplets using cascaded photon-pair sources. *Nature*, 466, 2010.

[19] K. Itoh, W. Watanabe, S. Nolte, and C. B. Schaffer. Ultrafastprocesses for bulk modification of transparent materials. *MRS BULLETIN*, 31, 2006.

[20] V. H. Kamrul. A femtosecond laser written integrated photonic chip for the heralded generation of ghz states. Master's thesis, Politecnico di Milano, 2021.

[21] E. Knill, R. Laflamme, and G. J. Milburn. A scheme for efficient quantum computation with linear optics. *Nature*, 409, 2001.

[22] P. Kok, W. J. Munro, K. Nemoto, T. C. Ralph, J. P. Dowling, and G. J. Milburn. Linear optical quantum computing with photonic qubits. *Review of Modern Physics*, 79, 2007.

[23] Y. Li, P. C. Humphreys, and S. C. B. Gabriel J. Mendoza. Resource costs for fault-tolerant linear optical quantum computing. *Physical Review X*, 5, 2015.

[24] P. Maazoldi, M. Nigro, and C. Voci. *Fisica volume II*. EdiSES s.r.l., 2017.

[25] A. Marcinkevicius, V. Mizeikis, S. Juodkazis, S. Matsuo, and H. Misawa. Effect of refractive index-mismatch on laser microfabrication in silica glass. *Applyed physics A*, 76, 2003.

[26] J. C. F. Matthews, A. Politi, A. Stefanov, and J. L. O'Brien. Manipulation of multiphoton entanglement in waveguide quantum circuits. *nature photonics*, 3, 2009.

[27] N. T. Nguyen, A. Saliminia, S. L. Chin, and R. Vallee. Control of femtosecond laser written waveguides in silica glass. *Applide Physics B*, 85, 2006.

[28] R. Osellame, G. Cerullo, and R. Rampon. *Femtosecond Laser Micromachining: Photonic and Microfluidic Devices in Transparent Materials*. Topics in applied physics, Springer-Verlag Berlin Heidelberg, 2012.

[29] F. L. Pedrotti and L. M. P. L. S. Pedrotti. *Introduction to Optics*. Pearson India, 2014.

[30] J. D. Plummer, M. D. Deal, and P. B. Griffin. *Silicon VLSI Technology: Fundamentals Practice and MOdeling*. Prentice Hall, inc., 2000.

[31] E. Polino, M. Riva, M. Valeri, R. Silvestri, G. Corrielli, A. Crespi, N. Spagnolo, R. Osellame, and F. Sciarrino. Experimental multiphase estimation on a chip. *Optica*, 6.

[32] R. Raussendorf and H. J. Briegel. A one-way quantum computer. *Physical Review Letter*, 86, 2001.

[33] R. Raussendorf, J. Harrington, and K. Goyal. A fault-tolerant one-way quantum computer. *Annals of physics*, 321, 2006.

[34] S. Richter, M. Heinrich, S. Döring, A. Tünnermann, S. Nolte, and U. Peschel. Nanogratings in fused silica: Formation, control, and applications. *JOURNAL OF LASER APPLICATIONS*, 24, 2012.

[35] M. Z. Rossi and F. Vismarra. *High-intensity lasers for nuclear and physical application*. Società Editrice Esculapio s.r.l., 2020.

[36] T. Rudolph. Why i am optimistic about the siliconphotonic route to quantum computing. *APL photonics*, 2, 2017.

[37] M. Sakakura, M. Shimizu, Y. Shimotsuma, K. Miura, and K. Hirao. Temperature distribution and modification mechanism inside glass with heat accumulation during 250 khz irradiation of femtosecond laser pulses. *Applied Physics Letters*, 93, 2008.

[38] P. Senellart, G. Solomon, and A. White. High-performance semiconductor quantum-dot single-photon sources. *Nature nanotechnology*, 12, 2017.

[39] A. W. Snyder and J. D. Love. *Optical waveguide theory*. chapman and hall. New York, 1983.

[40] K. Sugioka and Y. Cheng. *Femtosecond Laser 3D Micromachining for Microfluidic and Optofluidic Applications*. Springer, 2014.

[41] O. Svelto. *Principles of lasers*. Springer, 2010.

[42] A. Q. Tool. Relaxation of stresses in annealing glass. *RESEARCH PAPER RP1637, Part of Journal of Research of the National Bureau of Standards*, 34, 1945.

[43] T. M. Tritt. Thermoelectric materials: Principles, structure, properties, and applications. *Encyclopedia of Materials: Science and Technology*, 2002.

[44] M. Varnava, D. E. Browne, and T. Rudolph. Loss tolerance in one-way quantum computation via counterfactual error correction. *Physical Review Letter*, 97, 2006.

[45] M. Varnava, D. E. Browne, and T. Rudolph. How good must single photon sources and detectors be for efficient linear optical quantum computation? *Physical Review Letter*, 100, 2008.

[46] A. Zeilinger, M. A. Horne, H. Weinfurter, and M. Zukowski. Three-particle entanglements from two entangled pairs. *Physical Review Letters*, 78, 1997.

List of Figures

List of Tables

Acknowledgements

I have a lot of thanking to do, this work would not have been possible without all the people that I will acknowledge here.

First of all I want to thank Professor Roberto Osellame, for accepting my request to carry out my thesis work in its research group. I must also thank him for its beautiful course of *Quantum optics and information*, which made me really fond of these stimulating topics.

A big thanks goes to Hugo, my supervisor. He taught me how to perform all the procedures in the laboratory. He was always kind to me even if when I made some mistakes. Most importantly he made me really appreciate the life in the department and the research work.

I wish to thank Riccardo. Its open source library for python, *femto*, is really useful and well developed. It helped me a lot during all the fabrications and really simplified my work.

I want to thank every member of the *Osellami* research group, everyone was always available if I needed some help. Moreover the mood during the collective lunches or the coffee breaks was always enjoyable and this really improved my experience during all these months.

All these years of university culminated in this work. The road was long and I want to thank all my friends and colleagues that accompanied me and helped me in many different ways during this awesome period.

Last but not least the biggest thank goes to my family. They always supported me in my choices and truly made this possible.